Cobalt-enhanced Co x Fe 3− x O 4 photoanode for ultrafast photoelectrodegradation of organic dyes with integrated RSM optimization

Yassine Elaadssi, Véronique Madigou, Houssam Hajjoul, Madjid Arab

To cite this version:

Yassine Elaadssi, Véronique Madigou, Houssam Hajjoul, Madjid Arab. Cobalt-enhanced Co x Fe 3− x O 4 photoanode for ultrafast photoelectrodegradation of organic dyes with integrated RSM optimization. Catalysis Science & Technology, 2025, 15 (22), pp.6726 - 6743. ⟨10.1039/d5cy00951k⟩. ⟨hal-05391004⟩

HAL Id: hal-05391004
https://hal.science/hal-05391004v1

Submitted on 1 Dec 2025

View Article Online
View Journal

Catalysis Science & Technology

This article can be cited before page numbers have been issued, to do this please use: Y. Elaadssi, V. Madigou, H. Hajoul and M. Arab, *Catal. Sci. Technol.*, 2025, DOI: 10.1039/D5CY00951K.

ROYAL SOCIETY OF CHEMISTRY

rsc.li/catalysis

DOI: 10.1039/D5CY00951K

Cobalt-enhanced $Co_xFe_{3-x}O_4$ photoanode for ultrafast photoelectrodegradation of organic dyes with an integrated RSM optimization

Yassine Elaadssi[1], Véronique Madigou[1], Houssam Hajjoul[2], Madjid Arab[1].

[1] Université de Toulon, Aix Marseille Univ, CNRS, IM2NP, CS 60584, CEDEX 9, F-83041 Toulon, France.

[2] Université de Toulon, Aix Marseille Univ., CNRS, IRD, MIO, Toulon, France.

Abstract

In this work, two compositions of cobalt ferrite ($Co_xFe_{3-x}O_4$: x=1 and 1.5) were investigated as photoanodes for the photoelectrocatalytic (PEC) degradation of Rhodamine B. The structural and textural investigations confirmed the cubic spinel structure with monocrystalline grain size around 8 nm and high surface area (>100 m^2/g). The bandgap values of the samples, 2.32 eV (for x=1) and 2.18 eV (for x=1.5), enable visible light absorption and activation under sunlight. The catalytic results showed that complete degradation with a complete mineralization of rhodamine B was obtained. The RSM optimization studies allowed to identify the optimum degradation (100%) conditions in terms of Na_2SO_4 concentration, current density, initial RhB concentration and reaction time. The chemical trapping tests and redox potential study have confirmed that $OH^•$ and h^+ are the primary species driving the degradation process. Advanced characterizations were carried out to investigate the electrocatalytic and photo electrochemical properties. A high cobalt content improves the lifetime and charge carriers transfer and higher photogenerated electron-hole, confirming an enhancement in the photocatalytic potential. Photons with wavelengths corresponding to an energy higher than that of the bandgap allowed an efficient degradation (100% in 6 minutes). Furthermore, a comparative investigation of photocatalytic, electrocatalytic, and photo-electrocatalytic processes revealed a pronounced synergistic effect in the combined PEC system using $Co_xFe_{3-x}O_4$ spinel as photoanode.

View Article Online
DOI: 10.1039/D5CY00951K

1. Introduction

Wastewater contamination has become a critical environmental challenge, exacerbated by industrial discharges containing a wide range of pollutants. Among these, organic dyes pose a major problem due to their complex chemical structures, which make them highly resistant to natural degradation processes [1–5]. In particular, Rhodamine B is an organic dye widely found in wastewater because of its intensive use in textiles and other industries such as cosmetics and paper manufacturing. Its toxicity and high persistence contribute to major environmental negative impacts in aquatic environments. This emphasizes the critical need for more effective and sustainable wastewater treatment methods that go beyond the conventional approaches such as biological treatment [6], adsorption, and chemical oxidation [7]. The conventional approaches are often inadequate in terms of capacity, cost-effectiveness, and the prevention of secondary pollution. Consequently, advanced oxidation processes (AOP) such as photocatalysis have attracted attention due to their potential to efficiently degrade persistent organic pollutants [8,9]. During the AOP process, active species, capable of breaking down organic pollutants into harmless by-products [7,8,9], are produced when photocatalytic material is exposed to light [8,9]. To improve photocalytic performance, it is necessary to increase the lifetime of the charge carriers created in the material during exposure to light. In the photoelectrocatalytic process (PEC) an overpotential is applied to the sample which enhances the generation of charge carriers and increases their separation rate, thereby enhancing degradation performance. In the literature concerning PEC applications, studies typically focus on materials, classically used in photodegradation namely TiO_2, WO_3, ZnO, [12–14]. Few articles dealing with the photoelectrodegradation of rhodamine B, but some can be cited. J. Wu et al. [15] prepared TiO_2 nanotube arrays electrodes and showed that after 70 min almost complete degradation of rhodamine B is obtained for the best sample. In another example, for hierarchical TiO_2 nanonetwork-porous Ti hybrid [16], the maximum degradation of rhodamine B obtained was 85% after 60 min. Moreover, ZnO films elaborated by electrodeposition showed better results since nearly 100% of RhB degradation was obtained after 15 min of reaction time [17]. Due to their large bandgap,

View Article Online
DOI: 10.1039/D5CY00951K

these materials require UV radiation to be activated. To enable the use of visible light illumination, composites and heterojunctions based on TiO_2 and ZnO, as well as new materials are developed. Currently, a few materials used in photocatalysis under visible radiation are tested for the degradation of organic dyes: photoelectrocatalysis. ZnNiIn Layered Double Hydroxides used as photoelectrodes [18] were able to completely degrade a concentration of 20 mg/L of methylene blue in 3 hours. In this study, we explore a new PEC application by using cobalt ferrite spinel. While spinel ferrites such as cobalt ferrite ($CoFe_2O_4$) have attracted interest for standard photocatalysis, their potential as photoanodes in integrated PEC systems has been significantly less explored. We hypothesize that adjusting the Co/Fe ratio can strategically modify the material's band structure and charge carrier dynamics, leading to a more efficient photoanode for environmental applications. The photo-electrocatalytic performance depends not only on the synthesis conditions of the sample, which leads to different optical and photo-electrochemical properties [19–22], but also on the test conditions. As a result, a very large number of experiments over a long period is required to obtain the ideal conditions for effective degradation. For example, studying the influence of four parameters requires more than 600 experiments. To avoid this complexity, and reduce the number of experiments, statistical optimization methods are useful in this case. Response Surface Methodology (RSM), based on Central Composite Design (CCD), is a statistical approach used for the optimization of test parameters such as Na_2SO_4 concentration, current density, RhB concentration, and time. It also allows to evaluate the influence and interactions of these parameters on the process efficiency [23]. In this study, optimal conditions were defined as those that achieve the highest degradation in the shortest time, with a low applied current.

The photoelectrocatalytic behavior towards rhodamine B was tested under visible light radiation. To obtain information about the photogenerated charge carriers, photocurrent measurements were carried out. Additionally, this study investigates the impact of initial solution pH and the irradiation wavelength on degradation efficiency. To evaluate the synergistic effect, degradation experiments were conducted separately for photocatalysis (PC) and electrocatalysis (EC)

View Article Online
DOI: 10.1039/D5CY00951K

to compare them with the combined photoelectrocatalysis (PEC) process. Furthermore, to assess the extent of mineralization and to identify the primary reactive species involved in the degradation, Total Organic Carbon (TOC) analyses and scavenger tests were conducted.

Materials and Methods

2.1. Reagents and Precursors

Cobalt (II) nitrate hexahydrate ($Co(NO_3)_2.6H_2O$) and iron (III) nitrate nanohydrate $Fe(NO_3)_3.9H_2O$ were used as precursors and sources of metal ions. The pH was controlled by sodium hydroxide (NaOH). Cetyl-trimethyl-ammonium bromide (CTAB, 98+%) has been used as surfactant to control the morphology of the particles [24]. Rhodamine B ($C_{28}H_{31}ClN_2O_3$), L-ascorbic acid (ACS reagent, $\geq$ 99%), ethylene-diaminetetra-acetic acid disodium (EDTA), isopropanol (IPA) and indium tin oxide (ITO), were all purchased from Sigma-Aldrich. The reaction media was deionized water.

2.2. Structural and optical characterizations

Cobalt ferrite nanoparticles were synthesized using a hydrothermal method, synthesis details can be found in a previous work [24,25]. The obtained powders were analyzed by X-ray diffraction (EMPYREAN Panalytical diffractometer with Cu Kα radiation $\lambda = 1.5406$ Å). The scan interval was 10 - 80° using a step size of 0.028◦ and a scanning rate of 1°/min. The morphology and the chemical composition were investigated using a 200 kV FEI Tecnai G2 transmission electron microscope combined with an energy dispersive spectrometer (EDS). The specific surface area of $Co_xFe_{3-x}O_4$ were determined from a N_2 adsorption-desorption isotherm obtained at 77 K from (Autosorb-iQ, Quantachrome, USA). The UV–Vis diffuse reflectance spectra (DRS) were collected in the wavelength region of 200 to 800 nm by using a Shimadzu UV-1800 spectrophotometer [26]. The fluorescence (FL) and time-resolved fluorescence emission (TRF) measurements were performed using a Fluoromax fluorescence spectrophotometer from Horiba. For that, an excitation wavelength of 310 nm and an emission wavelength of 465 nm were used. The data decay curves were fitted to a biexponential function following Eq. 1 [27]:

$$I_t = I_1 {}_e^{-(t/\tau_1)} + I_2 {}_e^{-(t/\tau_2)} \qquad (1)$$

View Article Online
DOI: 10.1039/D5CY00951K

Here, I_1 and I_2 denote the intensities at different times of the decay, and τ_1 and τ_2 represent the respective lifetimes. Using Eq. 2, the lifetime of the carrier τ_{moy} was extracted [28]:

$$\tau_{moy} = \frac{(I_1\tau_1{}^2 + I_2\tau_2{}^2)}{(I_1\tau_1 + I_2\tau_2)} \qquad (2)$$

2.3. Preparation of $Co_xFe_{3-x}O_4$ electrode

For the electrochemical measurements, $Co_xFe_{3-x}O_4$ powders were deposited on ITO glass substrates through the drop casting method [29]. 5 mg of cobalt ferrite nanoparticles were dispersed in 2 mL of absolute ethanol and stirred for 15 min. Subsequently, 1 mL of the dispersion was dropped onto a 1×1 cm² ITO substrate and dried in an oven at 80°C for 2 hours, to ensure proper adhesion of the nanoparticles onto the substrate. These deposits, made for the two compositions, served as the working electrode (see Fig S1.a).

2.4. Photoelectrochemical Measurements

The photoelectrochemical measurements were carried out in a three-electrodes configuration using an OrigaLys electrochemical workstation (Fig. S1.b) [30]. Ag/AgCl electrode was employed as the reference electrode, while a platinum foil was used as the counter electrode. The working electrodes were $Co_xFe_{3-x}O_4$ deposits. The photoelectrochemical studies were performed in an electrolyte solution of 0.1 M sodium sulfate (Na_2SO_4). The Revoler Instytut Fotonowy LED was used for illumination [31]. This system allowed the wavelength of the incident light to be adjusted. Open-circuit potential (OCP) studies have been conducted under cycles of light-on and light-off to assess the equilibrium potential of the working electrode. The photovoltage can also be evaluated by the changes in potential upon light illumination provided by OCP studies. In addition, the photocurrent response technique used to measure the generated electric current has provided an indication of the photogeneration efficiency of charge carriers and its recombination dynamics. All the measurements were performed at an applied potential of 1.2 V, as this value guarantees a measurable photocurrent

View Article Online
DOI: 10.1039/D5CY00951K

signal. Besides the investigation of photocurrents, the resistance to charge carriers transfer was measured using electrochemical impedance spectroscopy (EIS) in Nyquist plot representation. All the EIS experiments were performed in a three-electrodes system, where a 5 mV AC signal was applied to the working electrode in a frequency range from 0.01 Hz to 100 kHz. In addition, Mott-Schottky tests were performed to evaluate the photocatalyst's electrochemical capacitance as a function of the applied potential at a constant frequency of 500 Hz. The flat-band potential was determined by plotting the inverse square of the capacitance versus the applied potential, which also reveals the type of $Co_xFe_{3-x}O_4$ semiconductors.

2.5. Photoelectrocatalytic Degradation Experiments

The photoelectrocatalytic degradation of Rhodamine B was investigated using the same OrigaLys electrochemical workstation system. The irradiation wavelength was 449 nm to ensure that both compositions are excited. The degradation process was monitored by measuring the decrease in absorbance at λ_{max} = 554 nm (main absorption band of RhB molecules) over the time, using a Shimadzu UV-1800 spectrophotometer. Samples (1ml) were collected at regular intervals (each minutes), and the photoelectrodegradation efficacy was calculated using the following equation (Eq. 3):

$$RhB_{PEC} = \frac{[RhB_0]-[RhB_t]}{[RhB_0]} \times 100 \qquad (3)$$

where $[RhB_0]$ and $[RhB_t]$ represent the concentration of the dye solution before and during the PEC process, respectively.

In addition, total organic carbon (TOC) analyses were performed to assess the degree of mineralization. The TOC analysis allowed the determination of the organic carbon content of the contaminated solution before and after the PEC treatment. By comparing the initial value (TOC_0) with the final value obtained after the degradation process (TOC_t), it was possible to estimate the mineralization of the rhodamine molecules. The percentage of TOC removal was calculated according to the following formula (Eq. 4):

$$\text{TOC removal (\%)} = \frac{TOC_0 - TOC_t}{TOC_0} \times 100 \qquad (4)$$

where TOC_0 is the measured value of the initial solution and TOC_t is the measured value after the PEC degradation process.

2.6. Measurement of Zero Charge Point

The point of zero charge (pH_{pzc}) corresponds to the value of pH solution for which the surface charge of the catalyst is neutral, with equivalent contributions from negative and positive surface groups. In order to determine this value, five values of pH were tested and for each 50 mg of $Co_xFe_{3-x}O_4$ was placed in beaker containing 50 mL of 0.1 M KNO_3 solution. The initial pH of these solutions was adjusted by the addition of 0.1 M HNO_3 or 0.1 M NaOH. Then the suspensions were left to equilibrate over 48 hours and the final pH values of the solution were measured after filtration. The pHpzc was subsequently determined from a plot of ΔpH (pHfinal - pHinitial) versus initial pH, as the initial pH value at which ΔpH equals zero [32].

2.7. Experimental design by response surface methodology

The optimization of RhB photo-electrodegradation test parameters was conducted using a Central Composite Design (CCD) model of Response Surface Methodology (RSM) [33]. In this work, four factors were set: current density, electrolyte concentration, RhB concentration, degradation time, with five value levels (Table. 1). To evaluate the effects of each parameter on RhB photoelectrocatalytic degradation a complete factorial plan, with 4 factors and 5 levels, requires a total of $5^4 = 625$ experiments. This is not a feasible solution from an economic and time point of view. Using RSM with CCD model, which can replace a full factorial plan, requiring significantly fewer experiments, the number of experiments is reduced to 29. This model still allows a complete evaluation of the linear, quadratic, and interaction effects of the factors but also allows to determine the optimal conditions to achieve a complete degradation in the shortest time and at a lower current density [34].

View Article Online
DOI: 10.1039/D5CY00951K

Table. 1: Experimental range and levels of factors for the RSM CCD optimization of $CoFe_2O_4$ PEC.

Factor	**Levels**				
	-2	**-1**	**0**	**+1**	**+2**
X_1: [Na_2SO_4] (mol/L)	0.1	0.15	0.20	0.25	0.3
X_2: Current density (mA/cm²)	1	2	3	4	5
X_3: [RhB_0] (ppm)	5	7.5	10	12.5	15
X_4: Time: (min)	3	6	9	12	15

The experimental data of the 29 tests were exploited using Nemrodw software, which generated a quadratic polynomial model (Eq. 5) to express the correlation between the response (Y = % RhB degradation) and the four independent variables [35]:

$$Y = \boldsymbol{b}_0 + \sum_{i=1}^{\mathbf{k}} \boldsymbol{b_i x_i} + \sum_{i=1}^{\mathbf{k}} \boldsymbol{b_{i-i} x_i^2} + \sum_{i=1}^{k-1} \sum_{j=i+1}^{k} \boldsymbol{b_{i-j} x_i x_j} + \boldsymbol{\varepsilon} \quad (5)$$

Here, b_0 represents the intercept term, b_i refers to the coefficients of the linear terms for each independent variable X_i, $b_{i\text{-}j}$ the interaction terms between pairs of variables, ε represents the model error. To compare the influences of independent variable X_i, these are coded and labelled as x_i (Eq. 6) gives the relation between raw and coded values: X_{i0} is midpoint value, and δ_{Xi} is the step size [35].

$$x_i = \frac{X_i - X_{i0}}{\delta X_i} \quad (6)$$

These terms permit to identify if there are synergistic or antagonistic interactions between factors. The validity of the models was checked by analysis of variance (ANOVA) with 95% confidence level. The 3D response surfaces and the 2D contour plots allowed the study of the interactions between the variables and facilitated the prediction of the optimal conditions for achieving the highest RhB degradation efficiency.

2. Results and discussion

View Article Online
DOI: 10.1039/D5CY00951K

3.1. Structural and textural investigations

In a previous work [8], we presented in detail a comprehensive characterization of the synthesized $Co_xFe_{3-x}O_4$ (x = 1 and 1.5) nanoparticles, related structural, morphological, optical, and electronic properties of the synthetized catalysts. The XRD analysis (Fig. 1a), reveals that both compositions crystallized in a single-phase cubic spinel (standard JCPDS datasheet n° 22-1086), with a shift of the peaks towards the higher angles for $Co_{1.5}Fe_{1.5}O_4$. This shift is due to a stronger substitution of Fe^{3+} cations by Co^{2+} cations in the spinel structure, the ionic radius of Co^{2+} being smaller, this results in a reduction of the lattice parameter. The average grain size was estimated using Debye-Scherrer method; it is 9 nm and 7 nm for x=1 and 1.5, respectively. As for the cell parameter, a higher cobalt content leads to a decrease in the size of the particles, phenomenon already reported in the literature [36].

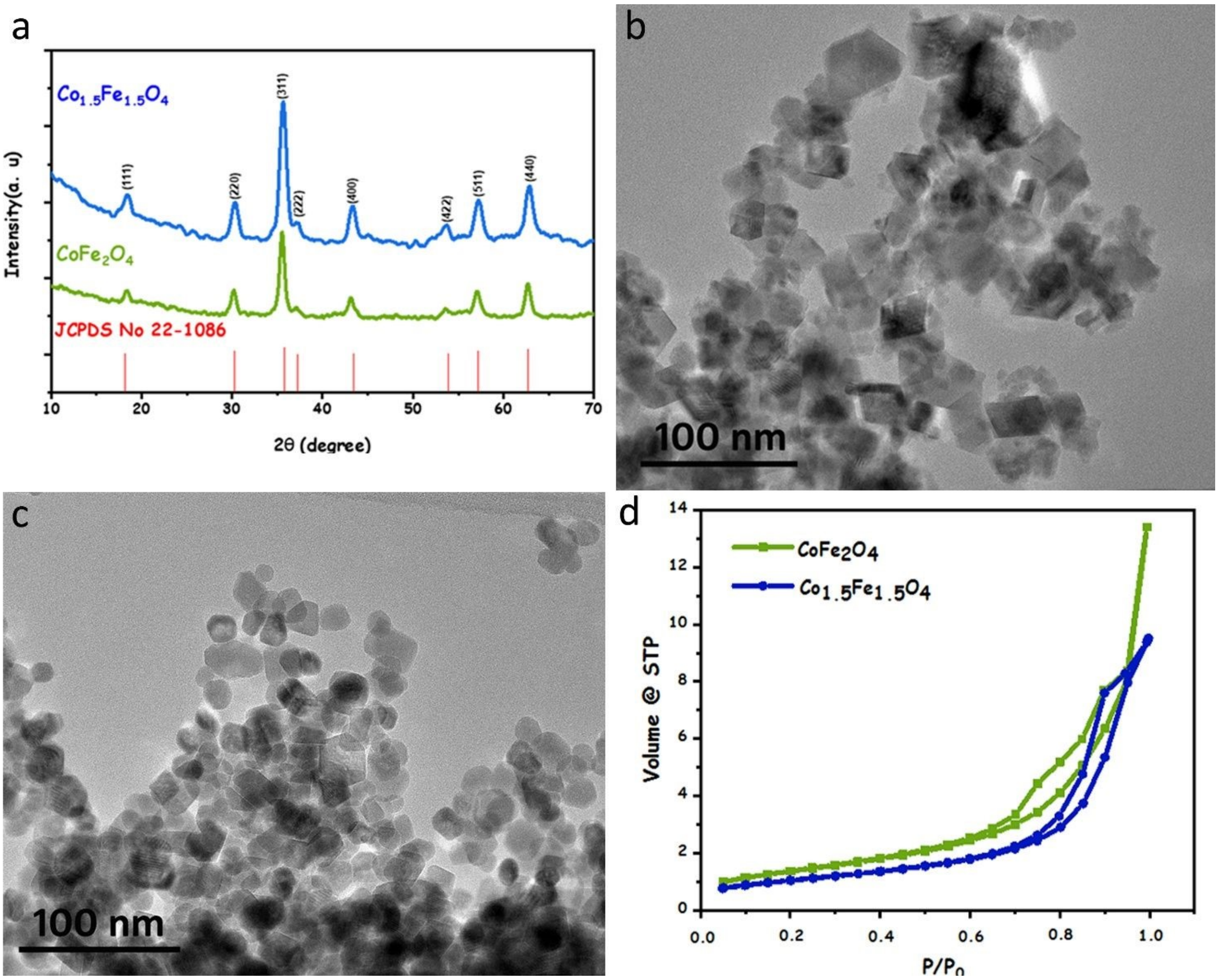

Fig. 1. a) X-ray diffraction diagrams, TEM micrographs of $Co_xFe_{3-x}O_4$ b) x=1 c) x=1.5, and d) Isotherms of N_2 adsorption-desorption the two samples

View Article Online
DOI: 10.1039/D5CY00951K

Transmission electron microscopy further supported these findings by showing well-defined nano-octahedral morphologies (TEM) (Fig. 1b-c). The histograms of the size distributions (insert Fig. S2), show a decrease in the average particle size from 9 nm for $CoFe_2O_4$ to 8 nm for $Co_{1.5}Fe_{1.5}O_4$. Since the particles are monocrystalline (see Fig. S2), the size of the particles corresponds to the crystalline one, so the values are in agreement with those deduced from the XRD data. To evaluate the chemical composition of the nanoparticles energy-dispersive spectroscopy was used. In this case we focused on the Fe/Co ratio (expressed in atomic percent) to extract the value of x in the $Co_xFe_{3-x}O_4$ formula. The results confirmed the expected elemental composition: $x = 0.92 \pm 0.08$ for $CoFe_2O_4$ and $x = 1.42 \pm 0.07$ for $Co_{1.5}Fe_{1.5}O_4$.

The surface characteristics of these materials were then studied by Brunauer–Emmett–Teller (BET) analysis. Fig. 1d shows the nitrogen adsorption and desorption isotherms of $CoFe_2O_4$ and $Co_{1.5}Fe_{1.5}O_4$ nanoparticles, they exhibit the characteristic features of type IV isotherms and typical H3 hysteresis loops according to IUPAC classification [37]. The appearance of such loops suggests the existence of mesoporous structures in materials [38,39]. Based on BET analysis (Fig. S3), both samples have close and high specific surface areas: 102 m²/g and 106 m²/g for x=1 and x=1.5, respectively. These values are much higher than the values usually reported in the literature for CoFe2O4 nanoparticles prepared by different methods (40 to 90 m²/g) [40,41]. This is a direct result of the small size of the nanoparticles obtained using hydrothermal syntheses, and their related surface area achieved from our synthetic protocol. The intrinsic relationship between particle size and specific surface area (SSA) for spherical particles can be described by the following equation: SSA = 6/ρ·D, where ρ is density of the material (~5.29 g/cm³) and D is diameter [42,42,43]. For comparison, a larger $CoFe_2O_4$ particle of 38 nm would have a theoretical SSA of ~30 m²/g, whereas for the ~8 nm particles produced in this work, the theoretical SSA is ~142 m²/g. The experimental value measured of ~106 m²/g statistically agrees with the theoretical value, supporting that high surface area is due to

View Article Online
DOI: 10.1039/D5CY00951K

small particle size. The successful synthesis of such small well dispersed nanoparticles was achieved by using CTAB as a surfactant to limit particle agglomeration and provide a larger number of exposed active sites for catalysis [44–46].

3.2. Optical and photoelectrochemical properties

The optical characteristics of $Co_xFe_{3-x}O_4$ nanoparticles were obtained by measuring the optical reflectance (R) by DRS and using the Kubelka-Munk function F(R) [8]. The bandgap energy was deduced with the Tauc plot method, based on the following equation (Eq. 7) and by plotting $(F(R)*h\nu)^{1/\gamma}$ versus $h\nu$ [47]:

$$(\alpha h\nu)^{1/\gamma} = B\,(h\nu - E_g) \qquad (7)$$

where α is the absorption coefficient, h is the Planck's constant, ν is the frequency of the light, E_g is the bandgap energy, B represents a constant, with γ being a function of the type of electronic transition (with γ = ½ for direct bandgap transitions) [48]. According to the DRS results (Fig. S4), $Co_{1.5}Fe_{1.5}O_4$ has a smaller bandgap of 2.18±0.02 eV than $CoFe_2O_4$ with a band gap of 2.32±0.05 eV. This reduction in the E_g can be due to the higher cobalt content which induces a decrease in atomic orbital interaction distances between O and Co. The polyhedral are then distorted which modifies the electronic structure of the samples. The extra Co^{2+} ions reduce the difference in energy between the valence band and the conduction band by changing the d-orbital energy distribution [49].

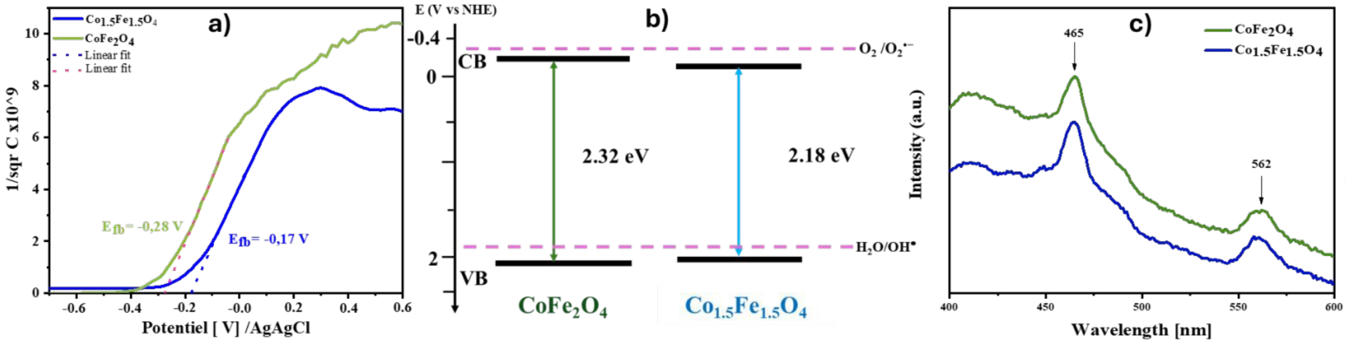

Fig. 2. a) Mott-Schottky graphs, b) representation of the VB and CB potential in the NHE scale for $CoFe_2O_4$ and $Co_{1.5}Fe_{1.5}O_4$ and c) fluorescence spectra of $Co_xFe_{3-x}O_4$.

View Article Online
DOI: 10.1039/D5CY00951K

Additionally, Mott-Schottky (MS) experiments on both compositions of the photo-electrocatalysts were conducted at 500 Hz to further define the band structure. The Mott-Schottky equation is given by (Eq. 8) [50]:

$$\frac{1}{\boldsymbol{C}^2} = \frac{2}{\boldsymbol{\varepsilon\varepsilon_0 A^2 \mathbf{e} N_D}}\left(\boldsymbol{V - V_{Fb} - \frac{k_B T}{\mathbf{e}}}\right) \qquad (8)$$

where C is the capacitance, N_D is the density of donors, e is the electron charge, ε is the relative permittivity, V is the applied potential, V_{FB} is the flat band potential, k_B represents Boltzmann's constant and T the absolute temperature. The linear part of the variation of $1/C^2$ with applied potential exhibits a positive slope in Mott-Schottky plot indicate that the two samples are n-type semiconductors [51–54]. The flat band potential (V_{FB}) can be determined by extrapolating the linear portion of the plot to zero [55]. Fig. 2a shows that the V_{FB} for $CoFe_2O_4$ and $Co_{1.5}Fe_{1.5}O_4$ is -0.28 V and -0.17 V vs. Ag/AgCl, respectively. From these values, the position of the E_{CB} for n-type semiconductors can be estimated. For this type of semiconductor electrode, it was assumed that the E_{CB} can be calculated via the relation (Eq. 9) [56]:

$$E_{CB} \approx V_{FB} - 0.2V \qquad (9)$$

Hence, the calculated E_{CB} values for $CoFe_2O_4$ and $Co_{1.5}Fe_{1.5}O_4$ are -0.48 V and -0.37 V vs. Ag/AgCl, respectively. corresponding to -0.28V and -0.17V vs. NHE [57]. Using the bandgap energies (E_g) determined from the DRS analysis, the valence band potential (E_{VB}) can be calculated using the relationship (Eq. 10) [58,59]:

$$E_{VB} = E_{CB} + E_g \qquad (10)$$

For $CoFe_2O_4$, with $E_g = 2.32$ eV, the E_{VB} is 2.04 eV vs. NHE and for $Co_{1.5}Fe_{1.5}O_4$, with $E_g = 2.18$ eV, the E_{VB} is 2.01 eV vs. NHE.

To investigate the electronic structures and to understand the charge dynamics, the fluorescence (FL) spectra of $CoFe_2O_4$ and $Co_{1.5}Fe_{1.5}O_4$ were recorded. As shown in Fig. 2c, there are some prominent peaks in the FL spectra of both samples. However, $CoFe_2O_4$ had a higher peak intensity than

View Article Online
DOI: 10.1039/D5CY00951K

$Co_{1.5}Fe_{1.5}O_4$, in particular, the principal peak at around 465 nm in the visible blue region of the spectra which can be attributed to the recombination of electron and hole pairs [60]. The higher intensity of FL is generally linked to more rapid recombination of photo-generated electron-hole pairs, which is not desired in photo-catalytic and photoelectrocatalytic applications, as it limits the charge carriers that are available for the catalytic reaction [61–63]. $Co_{1.5}Fe_{1.5}O_4$ photoelectrode showed a lower FL intensity compared to $CoFe_2O_4$, which indicates that electron-hole pair recombination is weaker, which leads to improved charge separation, likely attributable to defect states acting as traps [64]. The charge carrier lifetime has been measured by time-resolved fluorescence lifetime spectroscopy (Fig. S5), and it is 5.1 ns for $Co_{1.5}Fe_{1.5}O_4$, while it is shorter, 2.9 ns for $CoFe_2O_4$. The higher charge carrier lifetime for $x = 1.5$ implies that more electrons and holes are available to contribute to active radicals' formation. This may be due to an increase in charge diffusion at the surface of the material.

3.3. Optimization of the PEC process (RSM-CCD)

In this study the photoelectrochemical degradation of Rhodamine B was optimized using RSM_CDD. The number (N) of tests is given by the formula (Eq. 11) [65]:

$$N = 2^k + 2k + x_0 \qquad (11)$$

Where k is the number of factors and x_0 indicates the center point. The parameters of the degradation process that have been optimized in this work are Na_2SO_4 concentration (X_1), applied current density (X_2), initial dye concentration (X_3), and reaction time (X_4). The choice of these variables and their ranges is based on preliminary experiments that have been performed before applying RSM. The number of experiments in this case is 29, which represents 4 factors (k) and five 5 center points (x_0). Using Nemrowd software and based on the results of the Central Composite Design (CCD) experiments (Table S1), a quadratic model was developed to describe the relationship between the photoelectrochemical degradation (PEC) rate of Rhodamine B and the coded values of the experimental factors. The model equation is expressed as follows (Eq. 12):

View Article Online
DOI: 10.1039/D5CY00951K

$$\text{PEC }(\%) = 90.22 + 0.72\, x_1 + 4.18\, x_2 - 5.74\, x_3 + 7.53\, x_4 - 0.78\, x_1^2 - 4.51\, x_2^2 - 2.27\, x_3^2 - 3.96\, x_4^2$$
$$+ 7.68\, x_1x_2 - 2.17\, x_1x_3 + 2.86\, x_2x_3 - 1.12\, x_1x_4 + 0.03\, x_2x_4 + 1.48\, x_3x_4. \quad (12)$$

The model terms (b_i, b_{ii} and b_{ij}) with a p-value below 0.05 are considered significant and an analysis of variance was carried out to verify the significance of the proposed model (Table 2) [66].

The quality of the model fitting was evaluated using the determination coefficients R^2 and adjusted R^2 values. The high $R^2 = 0.99$ and adjusted $R^2 = 0.98$ values indicate that this model has a good fit to the experimental results and demonstrates good agreement between the observed and predicted values. Based on ANOVA, 14 of the 15 model terms were found to be statistically significant in influencing the degradation efficiency of RhB, with p-values less than 0.05. The interaction term between current density and time (b2b4) was the only term found to be not significant [67]. The interaction term b_2b_4 between current density and time was found to be not significant with a p-value of 0.756. The positive or negative values of the coefficients represent the synergistic or antagonistic effect of the parameter on the RhB degradation efficiency.

Table 2: Regression coefficients for the RSM CCD Model

Terms	Values	Standard deviation	p-values
Linear			
b0	90.22	0.15	<0.01***
b1	0.72	0.07	0.0399
b2	4.18	0.07	<0.01***
b3	-5.74	0.07	<0.01***
b4	7.53	0.07	<0.01***
Quadratic			
b1-1	-0.78	0.07	<0.0245
b2-2	-4.51	0.07	<0.01***
b3-3	-2.27	0.07	<0.01***
b4-4	-3.96	0.07	<0.01***
Interaction			
$b_{1\text{-}2}$	7.68	0.09	<0.01***
$b_{1\text{-}3}$	-2.17	0.09	<0.01***
$b_{1\text{-}4}$	-1.12	0.09	<0.0154
$b_{2\text{-}3}$	2.86	0.09	<0.01***
$b_{2\text{-}4}$	-0.03	0.09	0.756

b_{3-4}	1.48	0.09	<0.01***

View Article Online
DOI: 10.1039/D5CY00951K

According to the regression model and ANOVA results (Table 3), the degradation of RhB was influenced by all four factors: Na_2SO_4 concentration, current density, initial RhB concentration, and time. Particularly, the results revealed that time ($|b_4| = 7.53$) has the strongest effect on the degradation efficiency. Moreover, the effect of the RhB concentration (|b3| = 5.74) is slightly higher than current density (|b2| = 4.18) in the ranges chosen for each factor. For the electrolyte concentration (|b1| = 0.72) it was found to have a low impact on the PEC degradation. These results are supported by the generated 3D surface plots and 2D contour plots (Fig. S6). These plots indicate the interaction of the factors on RhB degradation, where time and RhB concentration are the most important parameters. The relative influence of each independent factor is visually summarized in Fig. 3. The steepness of the curves directly corresponds to the magnitude of the factor's effect. It is evident that reaction time has the strongest positive influence on degradation efficiency, while the initial RhB concentration has the most significant negative influence. The current density also has a strong positive effect. In contrast, the electrolyte concentration has a minimal impact on the outcome. These visual results are in excellent agreement with the coefficient values determined by ANOVA (Table 2).

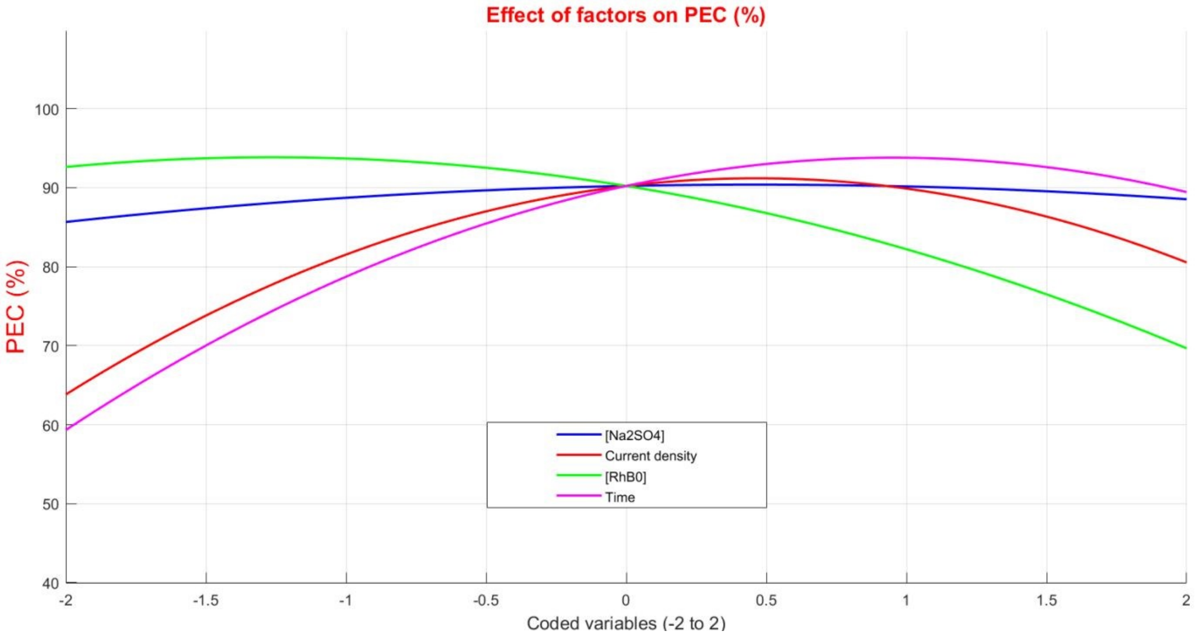

Fig. 3. The effect of each independent variable on RhB degradation efficiency.

View Article Online
DOI: 10.1039/D5CY00951K

The predicted optimal parameter values to achieve the highest degradation of RhB based on RSM-CCD modelling were Na_2SO_4 concentration: 0.26 mol L^{-1}, current density: 4 mA/cm², initial RhB concentration: 10.6 ppm and time: 10 min. The predicted degradation rate under these conditions is found to be 99.7%, which agrees with the experimental value of 100%, indicating that the model is able to accurately and reliably predict the best condition for RhB degradation using $CoFe_2O_4$ as catalyst.

3.4. Photo-electrocatalytic investigation of the $Co_xFe_{3-x}O_4$ photo-anode

3.4.1. Photo-electrocatalytic activity of $Co_xFe_{3-x}O_4$ in the optimum conditions

Under the optimal conditions determined by the RSM study (Na_2SO_4 concentration: 0.26 mol L^{-1}, current density: 4 mA/cm², initial RhB concentration: 10.6 ppm and time: 10 min), $CoFe_2O_4$ and $Co_{1.5}Fe_{1.5}O_4$ were compared in terms of their RhB photo-electrodegradation performances, with a wavelength irradiation of 449 nm. Fig. 4a represents the evolution of the UV-vis absorption spectra of the RhB solution over time using $CoFe_2O_4$. The decrease in the intensity of the main peak at 554 nm shows a complete degradation within 10 minutes, whereas for x= 1.5, the time is shorter: 6 minutes. Fig. 4b represents the ([RhB]/ [RhB_0]) ratio versus time ([RhB_0] is the initial concentration, [RhB] is the concentration at different times) obtained for photolysis, $CoFe_2O_4$ and $Co_{1.5}Fe_{1.5}O_4$, respectively. The photolysis experiment, which was conducted without a catalyst, showed that Rhodamine B is relatively stable when exposed to direct light, with only minimal degradation occurring during the monitoring period. For both samples, similar evolution was observed: a fast decrease of the RhB concentration in the first 4 minutes, then a slower decrease. After 4 minutes, $CoFe_2O_4$ achieved about 65% degradation, whereas $Co_{1.5}Fe_{1.5}O_4$ reached around 92%. The complete RhB degradation was obtained after 6 minutes for x=1.5, while the composition x=1 needed more time (9 minutes) to achieve a similar level of degradation. In addition, the evolution of Ln (([RhB]/ [RhB_0])) over time can be fitted by the Pseudo first-order kinetic model (Fig. 4c) in both cases. The kinetics investigation revealed that the rate constant of $Co_{1.5}Fe_{1.5}O_4$ (k = 0.558 min^{-1}) was almost

View Article Online
DOI: 10.1039/D5CY00951K

twice as high as that of $CoFe_2O_4$ (k = 0.306 min^{-1}), resulting in a faster degradation process with x= 1.5 than for x=1. These findings highlight the superior performance of highest cobalt content in the degradation of RhB.

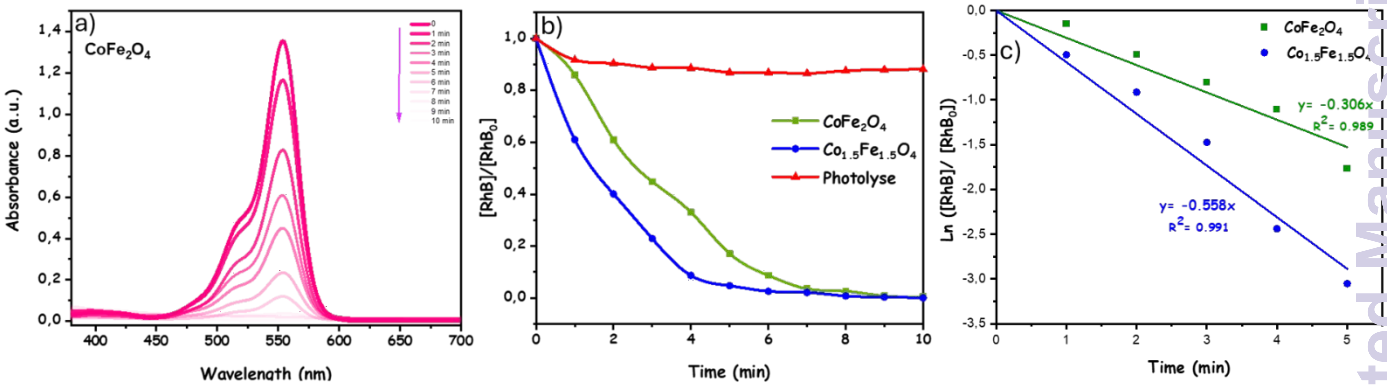

Fig. 4. a) UV-vis time-dependent absorption spectra of RhB solution with $CoFe_2O_4$ at native pH. b) Time variation of ([RhB]/ [RhB_0]) for photolysis and $Co_xFe_{3-x}O_4$ (x=1 and 1.5). c) Pseudo-first order kinetics fitted the Rhodamine B degradation.

3.4.2. Effect of electrolyte pH

In this investigation, the influence of the pH of the initial solution was studied: three different pH values (5, 6.5 and 9) were tested under the optimal process conditions previously identified (Na_2SO_4 concentration: 0.26 mol L^{-1}, current density: 4 mA/cm², initial RhB concentration: 10.6 ppm and time: 10 min). Fig. 5a shows the results for the x=1 composition. The degradation varies greatly with pH, becoming more pronounced as the pH increases. After 10 min, the degradation efficiency increased from 72% to 83% as the pH changed from 5 to 6.5. For a higher value, at pH= 9, the efficiency reached 100% at the same time. The study of the effect of pH for $Co_{1.5}Fe_{1.5}O_4$ reveals very similar trends to those observed for $CoFe_2O_4$. As shown in Fig 5b, the efficiency of degradation also changes substantially with the pH: at pH =5, the degradation efficiency after 10 minutes was 84%, increasing to 96% at pH= 6.5. At pH 9, an almost complete degradation was maintained within 6 minutes, demonstrating the catalyst's effectiveness in a basic medium. Both compositions showed improved degradation at higher pH levels. However, the effect of pH at basic conditions was more pronounced with $Co_{1.5}Fe_{1.5}O_4$. For instance, raising the pH from 5 to 9 increased the degradation of $CoFe_2O_4$ from approximately 51% to 82% after 5 minutes of reaction, whereas $Co_{1.5}Fe_{1.5}O_4$ increased

View Article Online
DOI: 10.1039/D5CY00951K

from around 54% to 100% under the same conditions. This improvement at a basic pH is due to an increased concentration of hydroxyl ions (OH^-), which deprotonate the catalyst's surface. This creates a more negatively charged surface, which enhances the electrostatic attraction and adsorption of cationic RhB molecules. This, in turn, facilitates their degradation. The interactions between the catalyst and the pollutant depend strongly on the surface charge of the catalyst and that of the pollutant. To control these interactions, it is necessary to determine the zero-point charge which is obtained from the curves of ΔpH as a function of the initial pH of the electrolyte (Fig 5c and 5d). The values of pH_{pzc} are slightly different 6.8 and 7.1 for x=1 and 1.5, respectively. The curves show the same type of variation, so the behavior at pH values below and above pH_{pzc} are similar. For $pH < pH_{pzc}$, the surface of the compound is positively charged, as Rhodamine B is a cationic dye, electrostatic repulsive forces occur with a maximum value for pH=5, which reduces the adsorption of RhB molecules on the catalyst surface. On the contrary, at $pH > pH_{pzc}$, due to the negatively charged surface of the compound, electrostatic attractions between the catalyst and the cationic dye are favored, which further facilitates the adsorption process. In basic environment, it can be noticed that $|\Delta pH|$ increases with the value of electrolyte pH, and the best results of degradation are obtained for pH= 9 (Fig 5a and 5b) for the two compositions.

View Article Online
DOI: 10.1039/D5CY00951K

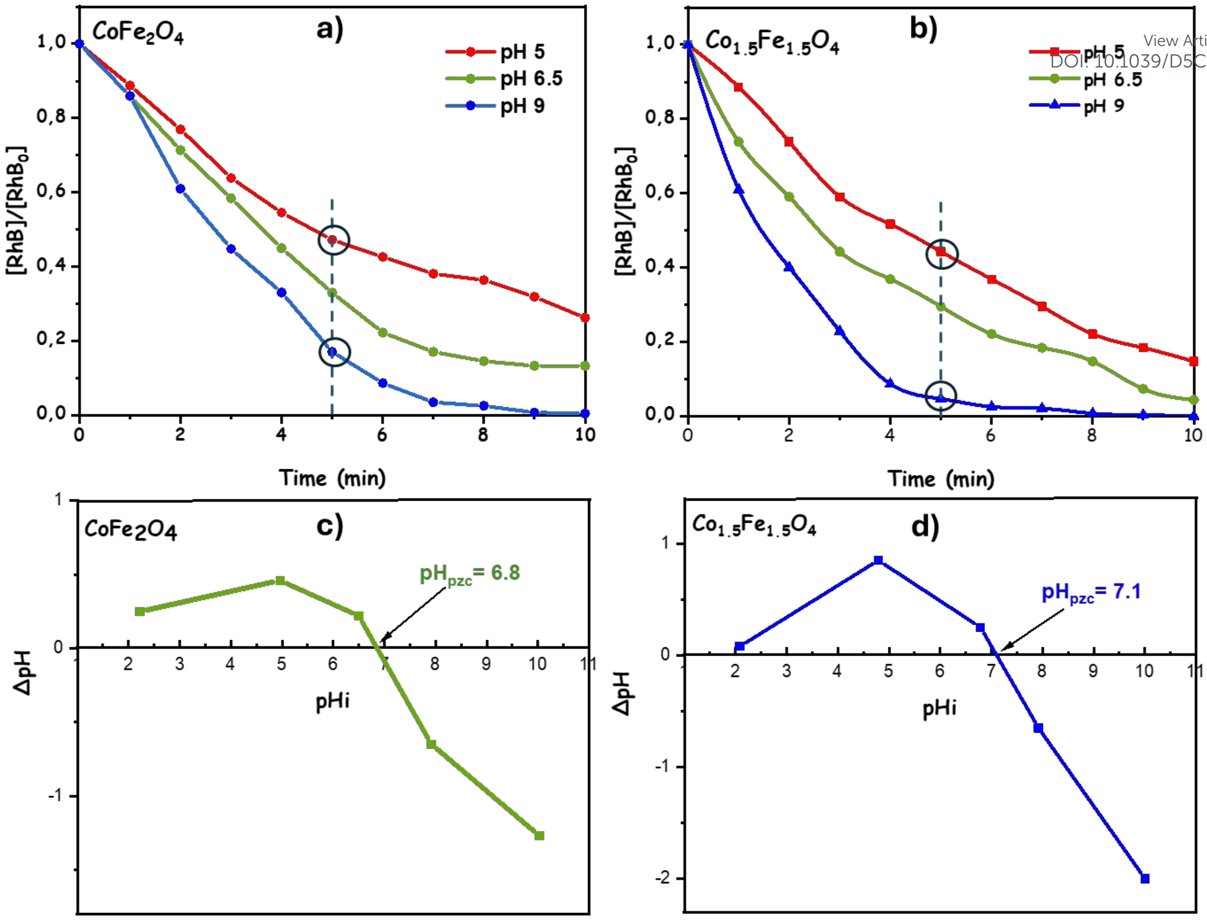

Fig. 5. The variation of [RhB]/ [RhB_0] ratio with the illumination time at different pH values for (a) $CoFe_2O_4$, (b) $Co_{1.5}Fe_{1.5}O_4$. Point zero charge plot (pH_{pzc}) for (c) $CoFe_2O_4$ and (d) $Co_{1.5}Fe_{1.5}O_4$.

3.4.3. Effect of wavelength on PEC degradation of RhB under optimal conditions.

In this part of the study, the influence of wavelength of irradiation on the PEC degradation of RhB was studied using $Co_{1.5}Fe_{1.5}O_4$. Different wavelengths, specifically 449 nm, 528 nm, 590 nm, and 736 nm, were tested under optimum conditions of process. Fig. 6 shows [RhB]/ [RhB_0] ratio over time, revealing two types of variation: on one side the results for the 449 nm and 528 nm wavelengths, and on the other side are those for the 590 nm and 736 nm wavelengths. With irradiation wavelengths of 449 nm and 528 nm, the system achieved nearly 100% of RhB degradation after 6 minutes of irradiation, which corresponds respectively to the photon energies of 2.76 eV and 2.35 eV. Moreover, when the higher wavelengths of 590 nm (2.10 eV) and 736 nm (1.69 eV) were used, the degradation efficiency reached only 80% after 10 minutes. The differences in the degradation ratio can be explained by considering the bandgap energies, for $Co_{1.5}Fe_{1.5}O_4$ E_g= 2.18 eV, so at wavelengths

View Article Online
DOI: 10.1039/D5CY00951K

corresponding to energy values above the energy gap (e.g. 449 nm and 528 nm), valence band electrons can be efficiently excited to move in the conduction band, allowing electron-hole pairs to form. On the other hand, at higher wavelengths (590 nm and 736 nm), corresponding energies are insufficient to photoactivate the $Co_{1.5}Fe_{1.5}O_4$ catalysis compound leading to less efficient photo-electro-degradation, which may be due only to the electrocatalytic contribution.

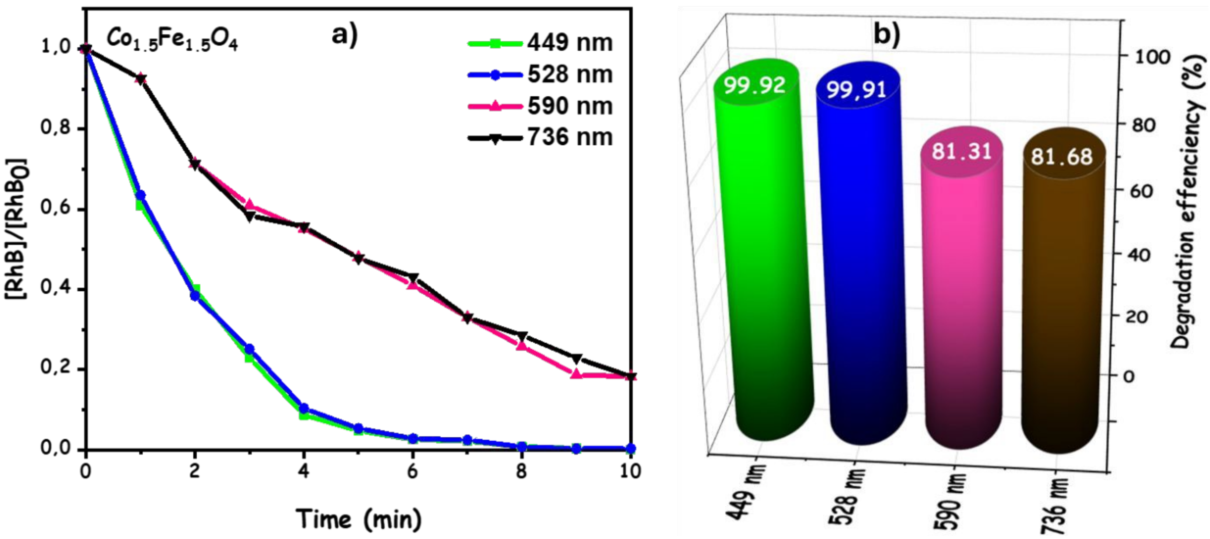

Fig. 6. a) The variation of $[RhB]/[RhB_0]$ with illumination time at different wavelength for $Co_{1.5}Fe_{1.5}O_4$ b) the corresponding degradation rate after 10 min at pH =9.

3.4.4. Synergistic Effect in Photoelectrocatalytic (PEC) Degradation

In order to assess the impact of the different sources of excitation as degradation process, photocatalytic (PC), electrochemical (EC), and photoelectrochemical (PEC) degradation of rhodamine B were performed under the optimized conditions of the process (4 $mA.cm^{-2}$, 0.26 $mol.L^{-1}$ of Na_2SO_4, and 10.6 ppm of rhodamine B using a 449 nm of irradiation source and a pH=9. Fig. 7a shows the $[RhB]/[RhB_0]$ variation over time with $Co_{1.5}Fe_{1.5}O_4$ as catalysts in the three cases. In the photocatalytic process (red curve), 44 % of RhB were degraded after 10 min, whereas in the electrocatalytic process (blue curve) the degradation efficiency achieved 83%. Moreover, for the same time of irradiation, complete RhB degradation was achieved (green curve) in the photoelectrochemical process. These results indicate that although single processes such as PC and EC are quite effective, the combination of photo-electro-catalytic process significantly enhances the

View Article Online
DOI: 10.1039/D5CY00951K

performance. The electro-degradation rate (EC) is in agreement with the previous values obtained in PEC process (see Fig. 6) with higher wavelengths of 590 nm (2.10 eV) and 736 nm (1.69 eV), suggesting the ineffectiveness of this irradiation to create charge carriers. However, the performance of the electrocatalytic process is higher than that of the photocatalytic process due to the influence of the external electric current. This external field is critical for enhancing the separation of charge carriers within the catalyst. During the EC process, the applied current allows to separate the charge carriers e^- and h^+, which prevents their recombination. This enhanced charge separation leads to a higher proportion of these charge carriers to generate active chemical species, which are important in the degradation of Rhodamine B. The analysis of the kinetics of the degradation curves, represented as ln ([RhB]/ [RhB_0]) versus time, showed that all the processes followed pseudo-first order kinetics, with rate constants as $|k| = 0.628\ min^{-1}$, $0.173\ min^{-1}$ and $0.061\ min^{-1}$ for PEC, EC and PC, respectively (Fig. 7b). The best improvement was achieved by the PEC process, with a constant rate of approximately 3.6 times higher than the EC and 10 times higher than PC (Fig. 7c).

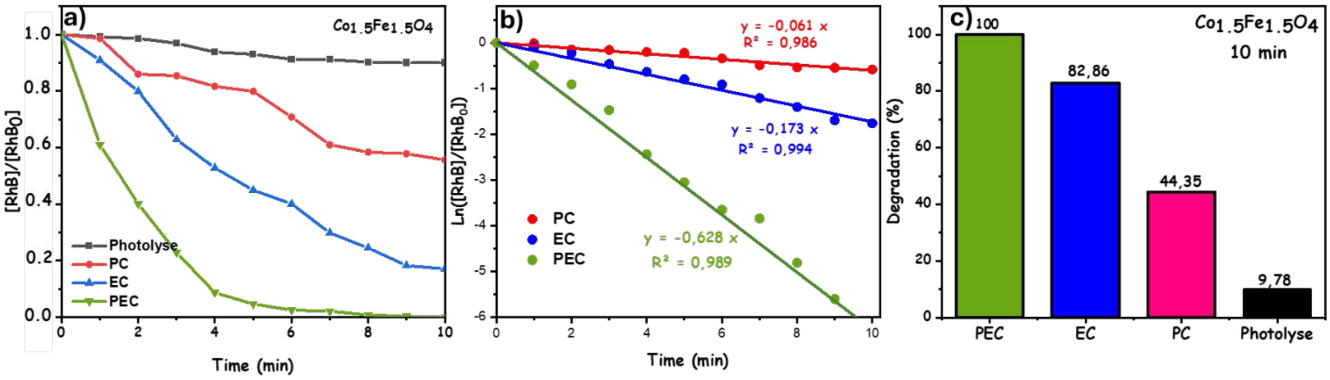

Fig. 7. a) Variations of the [RhB]/[RhB_0] ratio as a function of time for different processes pH 9. b) pseudo-first-order kinetic model for the decomposition of RhB using three processes. c) Comparative performance of photoelectrocatalysis, electrocatalysis, photocatalysis and photolysis by the decomposition of RhB over a reaction time of 10 min.

3.4.5. Stability and Reusability of the Photoanodes

The long-term stability and reusability of a photocatalyst are critical factors for its practical and economic viability in wastewater treatment applications. Therefore, to evaluate their operational stability, both photoanodes were tested over four consecutive cycles of RhB photoelectrodegradation.

View Article Online
DOI: 10.1039/D5CY00951K

Each cycle was run under the previously determined optimal test conditions. After each degradation experiment, the electrode was gently rinsed with deionized water and reintroduced into a fresh RhB solution for the next cycle. As illustrated in Fig. 8, for the $CoFe_2O_4$ photoanode, the degradation efficiency showed only a minor decrease, from 95% in the first cycle to about 90% in the fourth cycle. The $Co_{1.5}Fe_{1.5}O_4$ photoanode, which exhibited faster degradation kinetics, also maintained a high level of performance, with its efficiency decreasing from 100% to 96% over the same four cycles. To verify the integrity of the electrodes during the cycles, SEM observations were performed before and after the cycling tests (after 1 cycle and 4 cycles) (Fig. S7). No significant changes in the film's morphology were observed. The slight decrease in activity for both materials is probably due to the slight loss of material quantity from the catalyst deposit unavoidable during repeated handling. The good adhesion of the catalyst films to the ITO substrate and the intrinsic chemical robustness of the cobalt ferrite spinel structure under demanding photoelectrocatalytic conditions. To assess chemical stability and catalyst leaching, the reaction solution was analyzed by Inductively Coupled Plasma - Optical Emission Spectrometry (ICP-OES) after the final degradation cycle. For the superior-performing $Co_{1.5}Fe_{1.5}O_4$ photoanode, the measurements gave mass concentrations of cobalt and iron of 0.801 µg/L and 5.656 µg/L respectively. These low values of metal ions in the solution indicate that the leaching phenomenon through the cycles is negligible. The ability of both photoanodes to maintain high efficiency over multiple cycles is due to the high stability of the film and demonstrates the robustness of the photoanode for practical photoelectrodegradation applications.

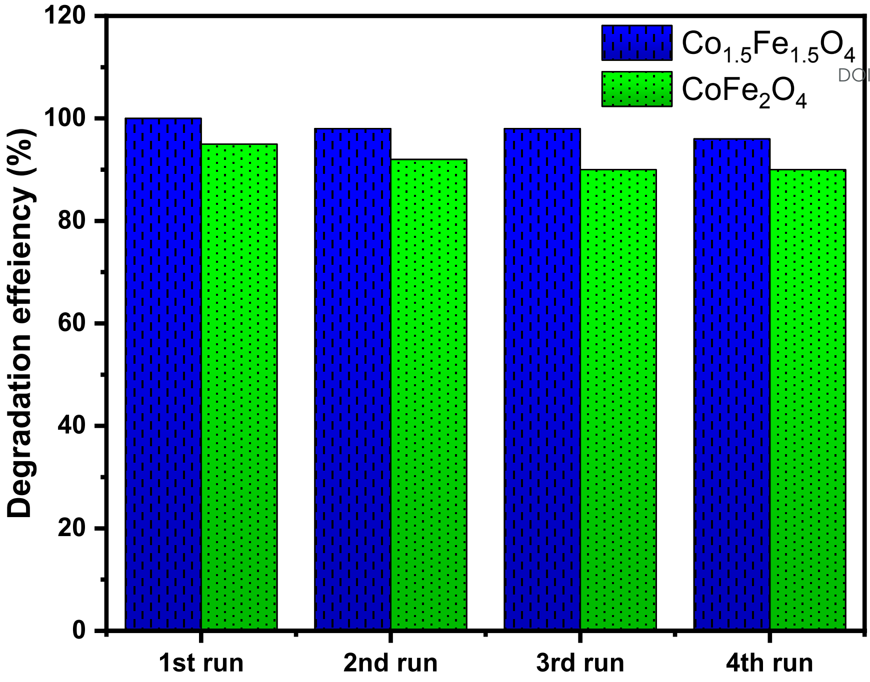

Fig.8: The recycling test using $CoFe_2O_4$ and $Co_{1.5}Fe_{1.5}O_4$ (measurements after 8 minutes).

3.4.6. Scavengers test

In the catalytic degradation of organic dyes, hydroxyl radicals ($OH^•$), superoxide radicals ($O_2^{•-}$) and holes (h^+) are considered to be the major active oxidative species involved in the degradation mechanism [68]. To investigate the degradation mechanisms of RhB using $Co_xFe_{3-x}O_4$ as photo-electrocatalyst, scavenging studies were carried out with different traps to determine the most active of these species. Isopropyl alcohol (IPA), L-ascorbic acid (L-asc) and ethylenediaminetetraacetic acid disodium (EDTA) were used to trap ($OH^•$), ($O_2^{•-}$) and (h^+), respectively [69]. The activities of these three species in the process were evaluated by experiments performed in the presence and absence of scavengers. A significant reduction in the degradation rate with the addition of a scavenger indicates that the corresponding trapped free radicals are active in the degradation mechanism. The results of the scavenger tests for RhB degradation with $Co_{1.5}Fe_{1.5}O_4$ are shown in Fig. 9, First, without the trapping agent, a complete degradation was reached in less than 8 minutes. The addition of ascorbic acid reduced the photoelectrodegradation efficiency to78%, indicating that the trapped superoxide radicals ($O_2^{•-}$) no longer participate in the degradation mechanism, which explains the loss of efficiency. Furthermore, isopropanol resulted in a degradation rate of 37%, meaning a higher

View Article Online
DOI: 10.1039/D5CY00951K

contribution of hydroxyl radicals ($OH^{\bullet}$) in the RhB degradation. Finally, the PEC efficiency fell to 9% when EDTA was used, confirming the major role of holes (h^+) in the degradation process. These results showed that the PEC degradation of RhB is mainly due to the synergistic effects of photogenerated hydroxyl radicals and holes in $Co_{1.5}Fe_{1.5}O_4$ photoelectrode, while the superoxide radicals have a minor role.

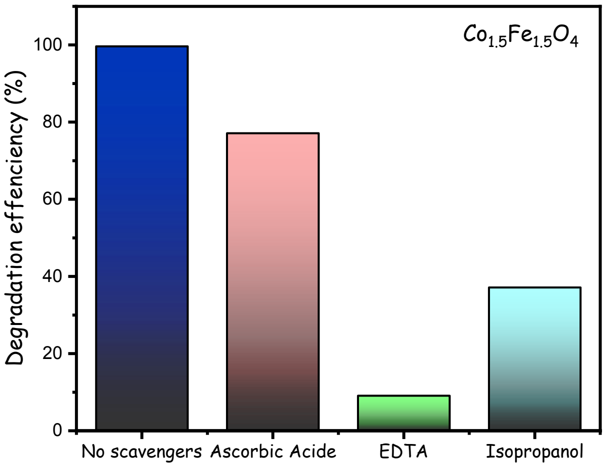

Fig. 9. Radicals trapping test using $Co_{1.5}Fe_{1.5}O_4$.

3.4.7. TOC Removal and Mineralization Efficiency:

Fig. 10 draws a parallel between the PEC degradation efficiency (obtained by UV-Vis absorbance spectroscopy) and the mineralization efficiency (calculated by Total Organic Carbon experiments) for both compositions (x=1 and x=1.5) after 10 minutes under the optimized conditions identified in this work. As can be seen above (see Fig 5a and 5b), in both catalysts' cases, the final concentration of rhodamine B detected by UV-Vis spectroscopy is zero, which means complete decolorization in 10 minutes. These discolored solutions were analyzed by the TOC method, which shows that, for x = 1, 95% of the organic carbon has disappeared and that there is practically no more organic carbon in the case of x= 1.5 (TOC removal = 99%). These results prove that the bonds of rhodamine molecules have been broken to give smaller molecules. The photoelectro degradation not only allows discoloration of the polluted solution but also the advanced mineralization of the rhodamine molecules.

View Article Online
DOI: 10.1039/D5CY00951K

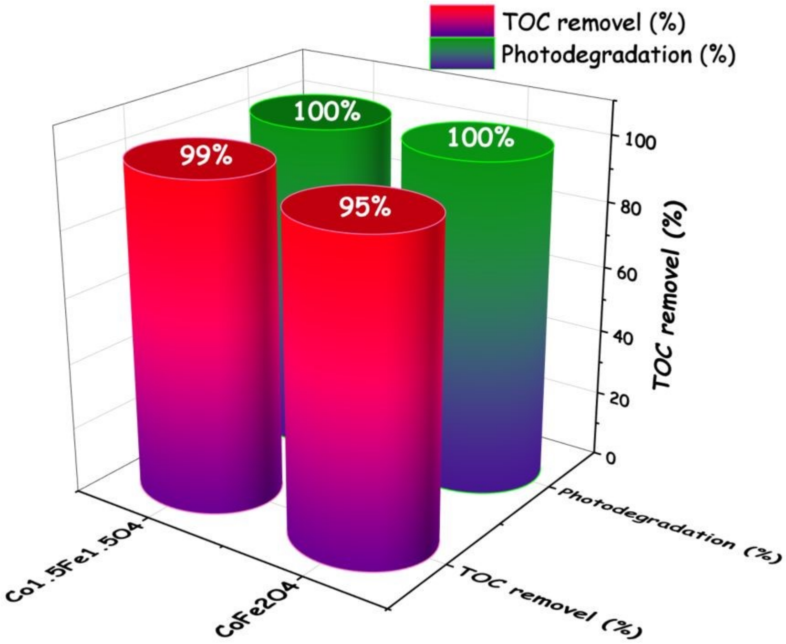

Fig. 10: TOC removal and PEC degradation of RhB using $Co_xFe_{3-x}O_4$ at pH 9.

3.5. Photoelectrochemical Studies

3.1.1. Electrochemical impedance spectroscopy (EIS)

The charge transfer at the $Co_xFe_{3-x}O_4$/electrolyte interface is responsible for the free radical's formation, and therefore of the PEC degradation. Electrochemical impedance spectroscopy (EIS) measurements were performed to evaluate the charge transfer resistance and presented in a Nyquist diagrams plot, in which the imaginary part of the impedance (Z") is plotted against the real part (Z'). In general, the diameter of the semicircle of the curves is correlated with the charge transfer resistance (R_{ct}) of the sample and gives an indication of the electrochemical process efficiency [70]. Fig. 11.a shows the Nyquist plots for both photoelectrodes materials, which have a similar semicircular shape, but their diameters are slightly different. In the case of $CoFe_2O_4$, the graph shows a wide semicircle (green curve), fitting the results yielded a charge transfer resistance (R_{ct}) of 3.3 kΩ.cm^{-2}. The $Co_{1.5}Fe_{1.5}O_4$ photoelectrode exhibits a smaller semicircle (blue curve), indicating a smaller charge transfer resistance, with a value of 2.8 kΩ.cm^{-2}. A high R_{ct} indicates a higher charge resistance at the electrode-electrolyte interface, which corresponds to a lower charge transfer rate. The R_{CT} reduced charge transfer resistance for x=1.5 reveals a better charge carrier mobility compared to x=1, indicating that the cobalt addition contributes to better separation and faster transport of the photogenerated electron-hole pairs through the interface [71].

View Article Online
DOI: 10.1039/D5CY00951K

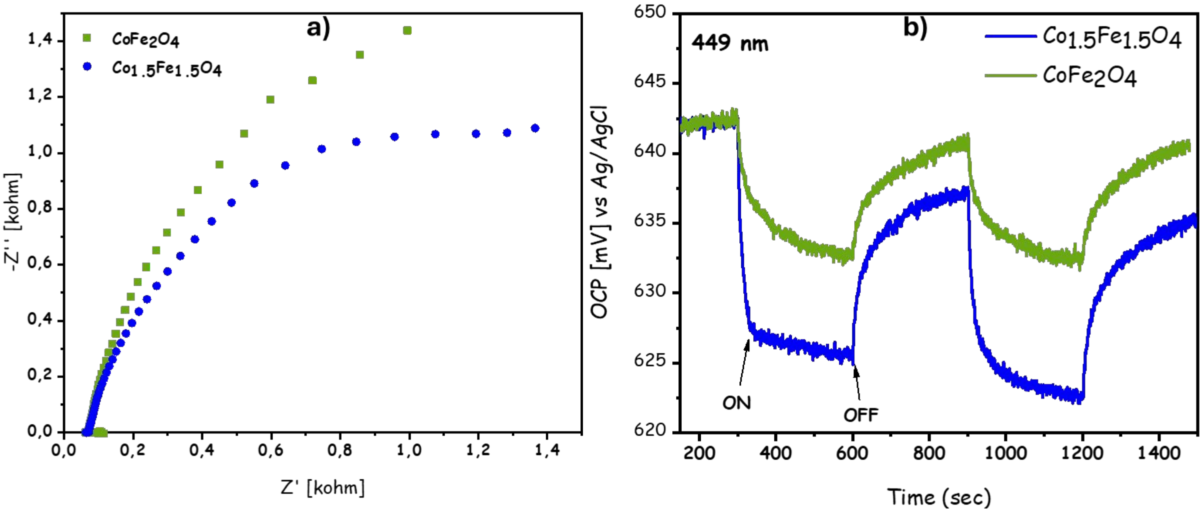

Fig. 11. a) EIS graphs and b) the OCP measurements at 449 nm.

3.1.2. Open-circuit potential (OCP)

In this study, the open-circuit potential measurements (OCP) in presence of the photocatalysts were evaluated in both dark and visible light illumination, as reported in Fig. 11.b. Under light exposure, the OCP for both samples shifted to the lower potential values, which indicates the mobility of the photogenerated electron-hole pairs within the materials [72,73]. The photovoltage (V_{ph}), defined as the difference between the OCP under illumination and the OCP in the dark [74], was higher for $Co_{1.5}Fe_{1.5}O_4$ with a value of 0.17V vs Ag/AgCl when compared to $CoFe_2O_4$ (0.11V vs Ag/AgCl). V_{ph} represents the maximum potential that a photocatalyst can produce under illumination without the application of an external voltage. A high value of photovoltage is advantageous for photo-electrochemical applications [75], because it allows more efficient charge transfer and improves reaction kinetics [76]. Moreover, it allows to reduce external bias potential necessary to apply to promote PEC degradation. The observed V_{ph} difference between $Co_{1.5}Fe_{1.5}O_4$ and $CoFe_2O_4$ may be due to the presence of cobalt rate, which potentially changes the cation distribution, improves the electronic structure and increases the light absorption capacity. This may also explain the superior PEC degradation results observed with $Co_{1.5}Fe_{1.5}O_4$.

3.1.3. Photocurrent response

View Article Online
DOI: 10.1039/D5CY00951K

The photocurrent measurements allow a direct evaluation of the photoelectrode's ability to photogenerate and maintain charge carriers under illumination. It reflects the effectiveness of charge separation and transport, which has a direct impact on catalytic performance [77,78].

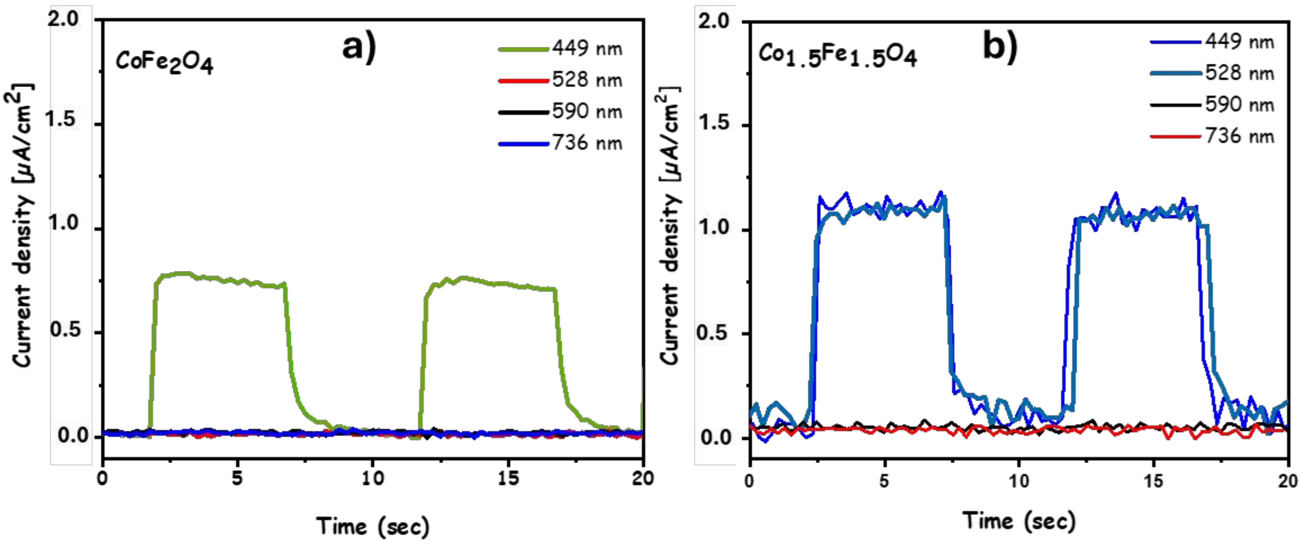

Fig. 12. Photocurrent responses of a) $CoFe_2O_4$ and b) $Co_{1.5}Fe_{1.5}O_4$ over different wavelengths of irradiation.

Samples photo-activation is assessed with different wavelengths: 449, 528, 590 and 736 nm. The photocurrent responses of the $CoFe_2O_4$ and $Co_{1.5}Fe_{1.5}O_4$ photo-electrocatalysts are shown in Fig. 12. For each sample and wavelength, two ON/OFF illuminations cycles were recorded. The results show that $CoFe_2O_4$ is photo-activated only by one wavelength: 449 nm (green curve) while $Co_{1.5}Fe_{1.5}O_4$ is activated by two wavelengths: 449 nm (dark blue curve) and 528 nm (light blue curve The photocurrent response of ITO, at 1.2 V applied potential and under 449 nm irradiation, is displayed in supplementary information (Fig. S8) along with the response of $Co_xFe_{3-x}O_4$ deposits (with x=1 and 1.5). When irradiated at 449 nm, no photocurrent response is observed for the ITO substrate, meaning that the energy applied is insufficient to activate ITO, given its wide bandgap reported in the range of between 3.5 and 4.3 eV [79-81]. The fact that the deposition for the composition x= 1 is activated only for one wavelength, while for x= 1.5 it is activated for two wavelengths comes from the respective values of gap energy. The bandgap energy of $CoFe_2O_4$ was evaluated to 2.32±0.05 eV and 2.18±0.02 eV for $Co_{1.5}Fe_{1.5}O_4$. The radiation at 449 nm naturally activates the two catalysts since it corresponds to an energy of 2.76 eV, a value higher than that of the two band gap energies. In the case of 528 nm radiation, corresponding to an energy of 2.35 eV, only $Co_{1.5}Fe_{1.5}O_4$ is activated. This lack of activation in $CoFe_2O_4$ occurs because the photon energy of 2.35 eV is too close to its absorption edge. This results in inefficient light absorption and insufficient generation of charge carriers, leading to a lack of significant photocurrent. For λ= 449nm, the photocurrent density during the light-on period of 0.75 µA/cm² for $CoFe_2O_4$ confirmed its ability to absorb visible light and generate hole-electron pairs. In contrast, the photocurrent density obtained for $Co_{1.5}Fe_{1.5}O_4$ was higher: 1.20 µA/cm², indicating that the increase of cobalt content in the ferrite led to an improvement in charge carrier generation. In addition, for both compositions, the stable photocurrent under light irradiation confirms the highly efficient charge separation.

3.6. Proposed Mechanism of Photoelectrodegradation of RhB Using $Co_xFe_{3-x}O_4$

This study shows that under visible radiation, the $Co_xFe_{3-x}O_4$ (x=1 and 1.5) cobalt ferrite photoanodes lead to the degradation of the rhodamine B (discoloration and mineralization). The process of photodegradation can be decomposed in several steps: · adsorption of the polluting molecules on the catalyst surface, ·· photogeneration of carrier charge by irradiation of the semiconductor, ··· charge carrier transport, ···· formation of reactive species [79]. By applying an overpotential on the electrode, the number of photogenerated charge carriers increases. The structural characteristics of the ferrite samples (grain size of 7-9 nm, surface areas around 100 m²/g) are favorable for the creation of a large number of active sites available for RhB molecule adsorption. In the same way, the gap energy values of the materials (2.32 and 2.18 eV) are such that they allow absorption of solar radiation to photoactivate the materials and generate charge carriers according to Eq.13. Afterwards, holes (h^+) oxidize H_2O molecules (Eq. 14), and electrons (e^-) interact with dissolved oxygen (Eq. 15) to form hydroxyl radicals ($OH^\bullet$) and superoxide($O_2^{\bullet-}$), respectively. The scavenger tests (Fig.9) have confirmed that $OH^\bullet$ and h^+ are the primary species driving the degradation process (Eq. 16) [80], while $O_2^{\bullet-}$ has a minor role (Eq. 17) [81].

$$Co_xFe_{3-x}O_4 + h\nu \rightarrow Co_xFe_{3-x}O_4\ (e^- + h^+) \qquad (13)$$

View Article Online
DOI: 10.1039/D5CY00951K

$$h^+ + H_2O \rightarrow OH^\bullet + H^+ \qquad (14)$$

$$e^- + O_2 \rightarrow O_2^{\bullet -} \qquad (15)$$

$$RhB + OH^\bullet \rightarrow CO_2 + H_2O + \text{intermediates} \qquad (16)$$

$$RhB + O_2^{\bullet -} \rightarrow CO_2 + H_2O + \text{intermediates} \qquad (17)$$

Furthermore, concerning the formation of active species, it is necessary to take into account the position of the VB and CB potential level in relation to those of the H_2O/ $OH^\bullet$ and $O_2/O_2^{\bullet -}$ redox couples (see Fig. 2b) which displays that the formation of active $OH^\bullet$ species is favored.

As can be seen on Fig. 7a showing a comparative performance of photoelectrocatalysis, electrocatalysis and photocatalysis, the highest performance was obtained for the PEC process (100% in 6 min). This high value is due to the synergistic impact of illumination (449 nm) and external polarization (4 $mA.cm^{-2}$), which can effectively reduce the recombination of photogenerated electron-hole pairs. These charge carriers have more time to form reactive species, which will degrade pollutant molecules. This results in enhanced generation of reactive oxygen species such as hydroxyl radicals, leading to faster degradation.

Based on photoelectrochemical measurements, band structure analysis, and the results from the scavenger tests, a possible mechanism for the photoelectrodegradation of RhB is proposed in Fig. 13. The $Co_xFe_{3-x}O_4$ catalyst absorbs photons of 449 nm wavelength and generates mobile electron-hole pairs. The current applied of 4 mA drives the photogenerated electrons towards the counter electrode, thereby improving charge separation and reducing electron-hole recombination. This efficient separation allows charges to migrate and react with water or oxygen to form highly reactive radicals ($O_2^{\bullet -}$ and $OH^\bullet$) which attack the RhB molecules. H. Fu *et al* [79] have shown by temporal proton NMR experiments that during the photocatalysis, destruction of RhB molecules by N-demethylation and/or the destruction of the conjugated structure of RhB, occurred. They have related these results to the TOC experiments, in which the carbon organic content decreases with the RhB concentration, thus proving its mineralization. The TOC results of this study (Fig. 10) present the same evolution with a residual carbon of 1 and 5% (respectively for x =1.5 and x = 1), in agreement with H. Fu et al [79]. We can therefore estimate that we have reached complete mineralization for x = 1.5.

This study pointed to another fact: increasing the cobalt content in the ferrite spinel greatly improves the photoelectrocatalytic properties of the material. The decrease of the band gap energy (from 2.32 to 2.18 eV), allowing more efficient light absorption in the visible region, improve carrier generation which results in higher photocurrent density. Moreover, the x=1.5 composition offers a lower charge transfer resistance (2.8 kΩ/cm² versus 3.3 kΩ/cm²), and a higher photovoltage under illumination, all of which contribute to efficient charge separation.

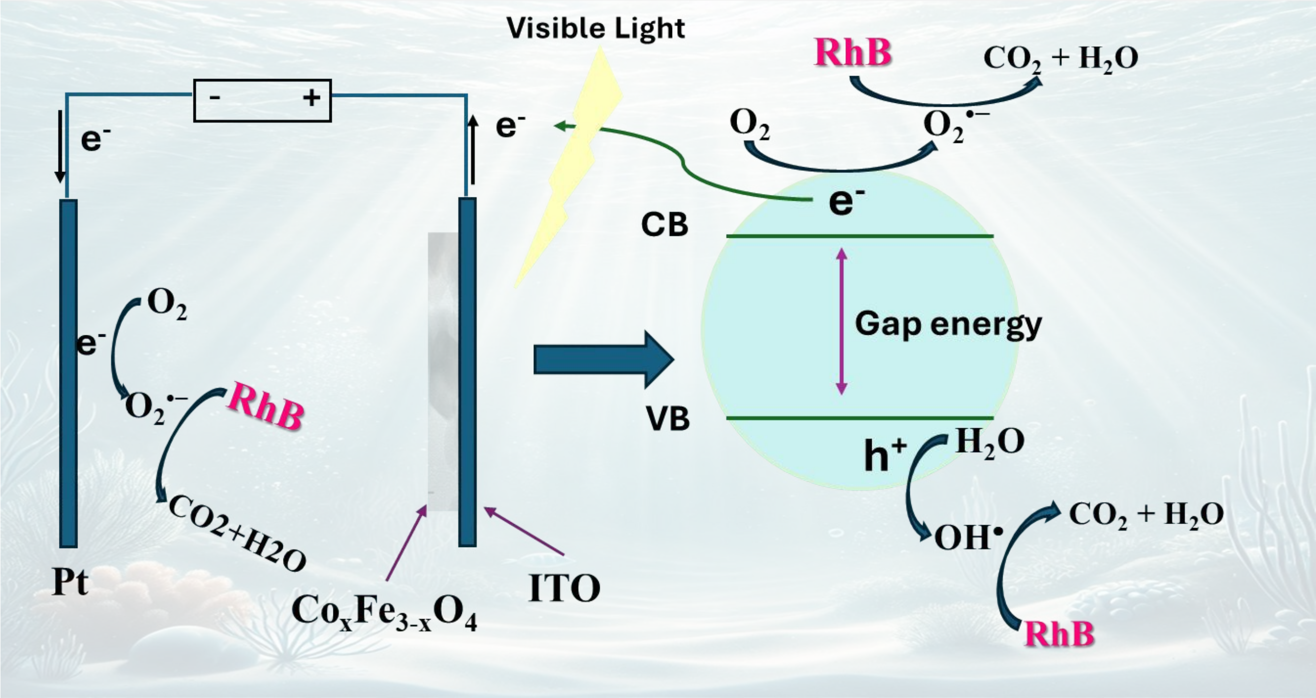

Fig. 13. The proposed mechanism for photo-electrodegradation of RhB using $Co_xFe_{3-x}O_4$.

A comparison of the individual degradation mechanisms showed that the pure EC and PC processes are less effective than the combined PEC method (Fig. 7a), which synergistically couples light absorption and external bias to promote recombination inhibition and reactive species production.

4. Conclusions

View Article Online
DOI: 10.1039/D5CY00951K

$Co_xFe_{3-x}O_4$ photoanodes were successfully tested for the complete photoelectrocatalytic degradation of Rhodamine B. Although the structural characteristics are similar for both compounds, i.e. nanometric monocrystalline grains (8-9 nm) with octahedral morphology and high specific surface area exceeding 100 m^2/g, increasing the cobalt content significantly alters the optical and photoelectrochemical properties. The Mott-Schottky method determined that the $Co_xFe_{3-X}O_4$ were n-type semiconductors, with a bandgap energy of 2.32±0.05 eV and 2.18±0.02 eV for x = 1 and x = 1.5, respectively. The photoelectrochemical studies, photocurrent and EIS, show that $Co_{1.5}Fe_{1.5}O_4$ presents better charge transfer capabilities and higher photogenerated electron-hole activity compared to $CoFe_2O_4$, confirming its improved photocatalytic potential. Furthermore, a dissociated study of the different activation sources of the x=1.5 compound, allowed us to estimate the real contribution of the photocatalysis (PC), and electrocatalysis (EC) mechanisms. The irradiation wavelength study on the PEC performance highlighted that photon energies exceeding that of their bandgap (449 nm and 528 nm), were essential for achieving high degradation efficiency (100% in 6 minutes). Conversely, lower energies (590 nm and 736 nm) were found to be ineffective, resulting in significantly reduced degradation (80% after 10 minutes), corresponding to the electrocatalytic contribution. In this way, the photoelectrocatalysis (PEC) reveals a pronounced synergistic effect, the combination of the two mechanisms leading to a complete degradation in a short time. The PEC process is 10 times faster than with the PC process and 3.6 times faster than with the EC process. To maximize the degradation percentage, the experimental test conditions were optimized using RSM-CCD model. Four parameters were considered (Na_2SO_4 concentration, current density, initial RhB concentration and reaction time) and the optimal values give a complete degradation (nearly 100% in 6 minutes). Investigation of the degradation mechanism based on the chemical trapping tests and bandgap structure studies have confirmed that $OH^{\bullet}$ and h^+ are the primary species driving the degradation process, with $O_2^{\bullet-}$ as a secondary species. Complementary organic carbon measurements (TOC) showed that in the case of x = 1.5 composition, 99% of rhodamine B molecules were mineralized in a short time. Cobalt ferrites are distinguished by their simple design and remarkable catalytic activity, enabling ultra-fast degradation under visible light radiation until mineralization. They are therefore the catalyst of choice for water treatment and have made it possible to achieve exceptionally efficient photoelectrodegradation of rhodamine B molecules.

Acknowledgements:

The authors gratefully acknowledge the Regional Council of Provence-AlpesCote d’Azur, Departmental Council of Var (CD83), the urban community of Toulon Provence Mediterranean and University of Toulon for their financial supports in the framework of the “NanoCat”, “Disolar” and “NSPEC” projects. For the SEM observations, the authors thank Damien Chaudanson from the CINaM – CNRS.

Conflicts of Interest: The authors declares that they have no known competing financial interest or personal relationships that could have appeared to influence the work reported in this paper.

References:

[1] L. Jin, Q. Tanzeel, U. Arif, F. Ali, N. Ali, C. Haotian, S. Mehmood, Y. Akbar, F. Raziq, Efficient photodegradation of organic dyes from industrial wastewater using novel Ni-decorated g-C3N4-TiO2 photocatalysts, Colloid Polym Sci 302 (2024) 487–502. https://doi.org/10.1007/s00396-023-05211-0.

[2] A. Tkaczyk, K. Mitrowska, A. Posyniak, Synthetic organic dyes as contaminants of the aquatic environment and their implications for ecosystems: A review, Science of The Total Environment 717 (2020) 137222. https://doi.org/10.1016/j.scitotenv.2020.137222.

[3] M. Ismail, K. Akhtar, M.I. Khan, T. Kamal, M.A. Khan, A. M. Asiri, J. Seo, S.B. Khan, Pollution, Toxicity and Carcinogenicity of Organic Dyes and their Catalytic Bio-Remediation, Current Pharmaceutical Design 25 (2019) 3645–3663. https://doi.org/10.2174/1381612825666191021142026.

[4] H. Zangeneh, A.A.L. Zinatizadeh, M. Habibi, M. Akia, M. Hasnain Isa, Photocatalytic oxidation of organic dyes and pollutants in wastewater using different modified titanium dioxides: A comparative review, Journal of Industrial and Engineering Chemistry 26 (2015) 1–36. https://doi.org/10.1016/j.jiec.2014.10.043.

[5] M. El Ouardi, V. Madigou, V. Chevallier, A. Merlen, A. BaQais, M. Saadi, H. Ait Ahsaine, M. Arab, Synthesis of ZnV2O6 nanosheet photocatalysts for efficient photodegradation of Rhodamine B: Experimental and RSM modeling, Journal of Environmental Chemical Engineering 12 (2024) 113505. https://doi.org/10.1016/j.jece.2024.113505.

[6] B.D. Tripathi, S.C. Shukla, Biological treatment of wastewater by selected aquatic plants, Environmental Pollution 69 (1991) 69–78. https://doi.org/10.1016/0269-7491(91)90164-R.

[7] P. Devi, U. Das, A.K. Dalai, *In-situ* chemical oxidation: Principle and applications of peroxide and persulfate treatments in wastewater systems, Science of The Total Environment 571 (2016) 643–657. https://doi.org/10.1016/j.scitotenv.2016.07.032.

[8] Y. Elaadssi, V. Madigou, M. Arab, Cobalt ferrites CoxFe3-xO4 (x = 1 and x = 1.5) as photocatalysts under simulated sunlight: An experimental study coupled to predictive RSM approach, Surfaces and Interfaces (2025) 106655. https://doi.org/10.1016/j.surfin.2025.106655.

[9] H. Liu, C. Wang, G. Wang, Photocatalytic Advanced Oxidation Processes for Water Treatment: Recent Advances and Perspective, Chemistry – An Asian Journal 15 (2020) 3239–3253. https://doi.org/10.1002/asia.202000895.

[10] F. Nandjou, S. Haussener, Degradation in photoelectrochemical devices: review with an illustrative case study, J. Phys. D: Appl. Phys. 50 (2017) 124002. https://doi.org/10.1088/1361-6463/aa5b11.

[11] J. Han, Y. Bian, X. Zheng, X. Sun, L. Zhang, A photoelectrochemical cell for pollutant degradation and simultaneous H2 generation, Chinese Chemical Letters 28 (2017) 2239–2243. https://doi.org/10.1016/j.cclet.2017.08.031.

[12] S. Wahyuningsih, C. Purnawan, T.E. Saraswati, E. Pramono, A.H. Ramelan, S. Pramono, A. Wisnugroho, Visible Light Photoelectrocatalytic Degradation of Rhodamine B Using Ti/TiO2-NiO Photoanode, Journal of Environmental Protection 5 (2014) 1630–1640. https://doi.org/10.4236/jep.2014.517154.

[13] M. Hepel, S. Hazelton, Photoelectrocatalytic degradation of diazo dyes on nanostructured WO3 electrodes, Electrochimica Acta 50 (2005) 5278–5291. https://doi.org/10.1016/j.electacta.2005.03.067.

[14] D. Wang, X. Li, J. Chen, X. Tao, Enhanced photoelectrocatalytic activity of reduced graphene oxide/TiO2 composite films for dye degradation, Chemical Engineering Journal 198–199 (2012) 547–554. https://doi.org/10.1016/j.cej.2012.04.062.

[15] J. Wu, K. Zhu, Y.F. Guo, H. Xu, W. Yan, Temperature Controlled Fabrication of TiO2 Nanotube-Based Arrays Electrode and Its Application for Photoelectrocatalytic Degradation of RhB, International Journal of Electrochemical Science 15 (2020) 1091–1107. https://doi.org/10.20964/2020.02.05.

[16] G.A. Cerrón-Calle, A.J. Aranda-Aguirre, C. Luyo, S. Garcia-Segura, H. Alarcón, Photoelectrocatalytic decolorization of azo dyes with nano-composite oxide layers of ZnO nanorods decorated with Ag nanoparticles, Chemosphere 219 (2019) 296–304. https://doi.org/10.1016/j.chemosphere.2018.12.003.

[17] A. Ait hssi, E. Amaterz, N. Labchir, L. Atourki, I.Y. Bouderbala, A. Elfanaoui, A. Benlhachemi, A. Ihlal, K. Bouabid, Electrodeposited ZnO Nanorods as Efficient Photoanodes for the Degradation of Rhodamine B, Physica Status Solidi (a) 217 (2020) 2000349. https://doi.org/10.1002/pssa.202000349.

[18] D. Pan, S. Ge, J. Zhao, J. Tian, Q. Shao, L. Guo, X. Mai, T. Wu, V. Murugadoss, H. Liu, T. Ding, S. Angaiah, Z. Guo, Synthesis and Characterization of ZnNiIn Layered Double Hydroxides Derived Mixed Metal Oxides with Highly Efficient Photoelectrocatalytic Activities, Ind. Eng. Chem. Res. 58 (2019) 836–848. https://doi.org/10.1021/acs.iecr.8b04829.

[19] M.E.K. Fuziki, R. Brackmann, D.T. Dias, A.M. Tusset, S. Specchia, G.G. Lenzi, Effects of synthesis parameters on the properties and photocatalytic activity of the magnetic catalyst TiO2/CoFe2O4 applied to selenium photoreduction, Journal of Water Process Engineering 42 (2021) 102163. https://doi.org/10.1016/j.jwpe.2021.102163.

[20] Y. Ortega López, H. Medina Vázquez, J. Salinas Gutiérrez, V. Guzmán Velderrain, A. López Ortiz, V. Collins Martínez, Synthesis Method Effect of CoFe2O4 on Its Photocatalytic Properties

View Article Online
DOI: 10.1039/D5CY00951K

for H2 Production from Water and Visible Light, Journal of Nanomaterials 2015 (2015) 985872. https://doi.org/10.1155/2015/985872.

[21] N.T. To Loan, N.T. Hien Lan, N.T. Thuy Hang, N. Quang Hai, D.T. Tu Anh, V. Thi Hau, L. Van Tan, T. Van Tran, CoFe2O4 Nanomaterials: Effect of Annealing Temperature on Characterization, Magnetic, Photocatalytic, and Photo-Fenton Properties, Processes 7 (2019) 885. https://doi.org/10.3390/pr7120885.

[22] M. Benlembarek, N. Salhi, R. Benrabaa, A.M. Djaballah, A. Boulahouache, M. Trari, Synthesis, physical and electrochemical properties of the spinel CoFe2O4: Application to the photocatalytic hydrogen production, International Journal of Hydrogen Energy 47 (2022) 9239–9247. https://doi.org/10.1016/j.ijhydene.2021.12.270.

[23] S. Sharma, A. Malik, S. Satya, Application of response surface methodology (RSM) for optimization of nutrient supplementation for Cr (VI) removal by *Aspergillus lentulus* AML05, Journal of Hazardous Materials 164 (2009) 1198–1204. https://doi.org/10.1016/j.jhazmat.2008.09.030.

[24] A.L. Lopes-Moriyama, V. Madigou, C.P.D. Souza, C. Leroux, Controlled synthesis of CoFe2O4 nano-octahedra, Powder Technology 256 (2014) 482–489. https://doi.org/10.1016/j.powtec.2014.01.080.

[25] L. Ajroudi, N. Mliki, L. Bessais, V. Madigou, S. Villain, Ch. Leroux, Magnetic, electric and thermal properties of cobalt ferrite nanoparticles, Materials Research Bulletin 59 (2014) 49–58. https://doi.org/10.1016/j.materresbull.2014.06.029.

[26] V. Manikandan, P. Velmurugan, P. Jayanthi, J.-H. Park, W.-S. Chang, Y.-J. Park, M. Cho, B.-T. Oh, Biogenic synthesis from Prunus × yedoensis leaf extract, characterization, and photocatalytic and antibacterial activity of TiO2 nanoparticles, Res Chem Intermed 44 (2018) 2489–2502. https://doi.org/10.1007/s11164-017-3242-7.

[27] H. Wang, M. Yu, C.K. Lin, J. Lin, Core–shell structured SiO2@YVO4:Dy3+/Sm3+ phosphor particles: Sol–gel preparation and characterization, Journal of Colloid and Interface Science 300 (2006) 176–182. https://doi.org/10.1016/j.jcis.2006.03.052.

[28] S. Murakami, M. Herren, D. Rau, M. Morita, Photoluminescence and decay profiles of undoped and Fe3+, Eu3+-doped PLZT ceramics at low temperatures down to 10 K, Inorganica Chimica Acta 300–302 (2000) 1014–1021. https://doi.org/10.1016/S0020-1693(00)00008-6.

[29] P.R. Somani, S.P. Somani, S.P. Lau, E. Flahaut, M. Tanemura, M. Umeno, Field electron emission of double walled carbon nanotube film prepared by drop casting method, Solid-State Electronics 51 (2007) 788–792. https://doi.org/10.1016/j.sse.2007.02.041.

[30] Instrument Électrochimique Multi-Voies avec Impédance | Origalys, (n.d.). https://www.origalys.com/PBCPPlayer.asp?ID=2357914 (accessed November 29, 2024).

[31] Rewolwer LED, Instytut Fotonowy (n.d.). https://www.fotonowy.pl/produkty/rewolwer-led/ (accessed November 29, 2024).

[32] M. Al-Harahsheh, R. Shawabkeh, A. Al-Harahsheh, K. Tarawneh, M.M. Batiha, Surface modification and characterization of Jordanian kaolinite: Application for lead removal from aqueous solutions, Applied Surface Science 255 (2009) 8098–8103. https://doi.org/10.1016/j.apsusc.2009.05.024.

[33] A. Amri, Z. Zulfansyah, M.I. Fermi1, I. Sulistyati, MODELING, VARIABLES INFLUENCE AND OPTIMIZATION USING RESPONSE SURFACE METHOD - CENTRAL COMPOSITE DESIGN (RSM-CCD) ON THE SODIUM LIGNOSULFONATE PRODUCTION FROM PALM OIL STEM BIOMASS, in: 2009: pp. 1–6. http://eprints.undip.ac.id/6179/ (accessed November 27, 2024).

[34] H. Pashaei, A. Ghaemi, M. Nasiri, B. Karami, Experimental Modeling and Optimization of CO2 Absorption into Piperazine Solutions Using RSM-CCD Methodology, ACS Omega 5 (2020) 8432–8448. https://doi.org/10.1021/acsomega.9b03363.

[35] S. Merabet, A. Bouzaza, M. Bouhelassa, D. Wolbert, Modélisation et optimisation de la photodégradation du 4-méthylphénol dans un réacteur à recirculation en présence d'UV/ZnO, rseau 22 (2009) 565–573. https://doi.org/10.7202/038331ar.

[36] S. Saddeler, G. Bendt, S. Salamon, F.T. Haase, J. Landers, J. Timoshenko, C. Rettenmaier, H.S. Jeon, A. Bergmann, H. Wende, B.R. Cuenya, S. Schulz, Influence of the cobalt content in cobalt iron oxides on the electrocatalytic OER activity, J. Mater. Chem. A 9 (2021) 25381–25390. https://doi.org/10.1039/D1TA06568H.

[37] M. Thommes, K. Kaneko, A.V. Neimark, J.P. Olivier, F. Rodriguez-Reinoso, J. Rouquerol, K.S.W. Sing, Physisorption of gases, with special reference to the evaluation of surface area and pore size distribution (IUPAC Technical Report), Pure and Applied Chemistry 87 (2015) 1051–1069. https://doi.org/10.1515/pac-2014-1117.

[38] A. Nasiri, M. Malakootian, M.R. Heidari, S.N. Asadzadeh, CoFe2O4@Methylcelloluse as a New Magnetic Nano Biocomposite for Sonocatalytic Degradation of Reactive Blue 19, J Polym Environ 29 (2021) 2660–2675. https://doi.org/10.1007/s10924-021-02074-w.

[39] R. Tabit, O. Amadine, Y. Essamlali, K. Dânoun, A. Rhihil, M. Zahouily, Magnetic $CoFe_2O_4$ nanoparticles supported on graphene oxide ($CoFe_2O_4$/GO) with high catalytic activity for peroxymonosulfate activation and degradation of rhodamine B, RSC Adv. 8 (2018) 1351–1360. https://doi.org/10.1039/C7RA09949E.

[40] S. Omidi, A.M. Davarpanah, A.R. Abbasian, Enhancement of specific surface area of CoFe2O4 powders synthesized by KCl-assisted solution combustion: effect of KCl content and initial pH, Iranian Journal of Physics Research 22 (2022) 353–371. https://doi.org/10.47176/ijpr.22.2.61266.

[41] M. Safari, J. Mazloom, Electrochemical performance of spindle-like Fe2Co-MOF and derived magnetic yolk-shell CoFe2O4 microspheres for supercapacitor applications, J Solid State Electrochem 25 (2021) 2189–2200. https://doi.org/10.1007/s10008-021-04989-9.

[42] K.S. Lim, H. Nersisyan, S.K. Han, K.-T. Park, H. Suh, J.H. Lee, Thermochemical response of TiO2 upon heating with CaMg2 reductant: Experimental findings and theoretical modeling, Next Materials 8 (2025) 100803. https://doi.org/10.1016/j.nxmate.2025.100803.

[43] A.C. Popa, G.E. Stan, M.A. Husanu, I. Mercioniu, L.F. Santos, H.R. Fernandes, J.M.F. Ferreira, Bioglass implant-coating interactions in synthetic physiological fluids with varying degrees of biomimicry, IJN 12 (2017) 683–707. https://doi.org/10.2147/IJN.S123236.

[44] G.C. Carvalho, G.D. Marena, J.C.F. Karnopp, J. Jorge, R.M. Sábio, M.A.U. Martines, T.M. Bauab, M. Chorilli, Cetyltrimethylammonium bromide in the synthesis of mesoporous silica nanoparticles: General aspects and *in vitro* toxicity, Advances in Colloid and Interface Science 307 (2022) 102746. https://doi.org/10.1016/j.cis.2022.102746.

[45] C. Italiano, N.T.J. Luchters, L. Pino, J.V. Fletcher, S. Specchia, J.C.Q. Fletcher, A. Vita, High specific surface area supports for highly active Rh catalysts: Syngas production from methane at high space velocity, International Journal of Hydrogen Energy 43 (2018) 11755–11765. https://doi.org/10.1016/j.ijhydene.2018.01.136.

[46] G. Kesavan, M. Pichumani, S.-M. Chen, C.-S. Ko, Surfactant-assisted (CTAB, PVA, PVP) thermal decomposition synthesis of strontium spinel ferrite nanocrystals for electrochemical sensing of cytostatic drug flutamide, Materials Today Chemistry 26 (2022) 101045. https://doi.org/10.1016/j.mtchem.2022.101045.

[47] S. Landi, I.R. Segundo, C. Afonso, O. Lima, M.F.M. Costa, E. Freitas, J. Carneiro, Evaluation of band gap energy of TiO2 precipitated from titanium sulphate, Physica B: Condensed Matter 639 (2022) 414008. https://doi.org/10.1016/j.physb.2022.414008.

[48] P. Makuła, M. Pacia, W. Macyk, How To Correctly Determine the Band Gap Energy of Modified Semiconductor Photocatalysts Based on UV–Vis Spectra, J. Phys. Chem. Lett. 9 (2018) 6814–6817. https://doi.org/10.1021/acs.jpclett.8b02892.

View Article Online
DOI: 10.1039/D5CY00951K

[49] A. Azouaoui, M. El Haoua, S. Salmi, A. El Grini, N. Benzakour, A. Hourmatallah, K. Bouslykhane, Structural and Magnetic Properties of Cd–Co Ferrites: Density Functional Theory Calculations and High-Temperature Series Expansions, J Supercond Nov Magn 33 (2020) 1831–1838. https://doi.org/10.1007/s10948-020-05429-x.

[50] A. Adán-Más, T.M. Silva, L. Guerlou-Demourgues, M.F. Montemor, Application of the Mott-Schottky model to select potentials for EIS studies on electrodes for electrochemical charge storage, Electrochimica Acta 289 (2018) 47–55. https://doi.org/10.1016/j.electacta.2018.08.077.

[51] N. Labchir, A. Hannour, A.A. Hssi, D. Vincent, K. Abouabassi, A. Ihlal, M. Sajieddine, Synthesis and characterization of CoFe2O4 thin films for solar absorber application, Materials Science in Semiconductor Processing 111 (2020) 104992. https://doi.org/10.1016/j.mssp.2020.104992.

[52] R. Nasser, H. Zhou, H. Elhouichet, S. Melhi, Z. Li, J.-M. Song, NiFe2O4@NiCo2O4 hollow algae-like microspheres enabled by Mott-Schottky for electrochemical energy storage, Chemical Engineering Journal 489 (2024) 151554. https://doi.org/10.1016/j.cej.2024.151554.

[53] X. Zhang, J. Zhang, Z. Ma, L. Wang, K. Yu, Z. Wang, J. Wang, B. Zhao, Ag engineered NiFe-LDH/NiFe2O4 Mott-Schottky heterojunction electrocatalyst for highly efficient oxygen evolution and urea oxidation reactions, Journal of Colloid and Interface Science 665 (2024) 313–322. https://doi.org/10.1016/j.jcis.2024.03.124.

[54] N. Labchir, E. Amaterz, A. Hannour, A. Ait hssi, D. Vincent, A. Ihlal, M. Sajieddine, Highly efficient nanostructured CoFe2O4 thin film electrodes for electrochemical degradation of rhodamine B, Water Environment Research 92 (2020) 759–765. https://doi.org/10.1002/wer.1272.

[55] A. Hankin, F.E. Bedoya-Lora, J.C. Alexander, A. Regoutz, G.H. Kelsall, Flat band potential determination: avoiding the pitfalls, J. Mater. Chem. A 7 (2019) 26162–26176. https://doi.org/10.1039/C9TA09569A.

[56] M. El Ouardi, O. Ait Layachi, E. Amaterz, A. El Idrissi, A. Taoufyq, B. Bakiz, A. Benlhachemi, M. Arab, A. BaQais, H. Ait Ahsaine, Photo-electrochemical degradation of rhodamine B using electrodeposited Mn3(PO4)2.3H2O thin films, Journal of Photochemistry and Photobiology A: Chemistry 444 (2023) 115011. https://doi.org/10.1016/j.jphotochem.2023.115011.

[57] C. Feng, Z. Lu, Y. Zhang, Q. Liang, M. Zhou, X. Li, C. Yao, Z. Li, S. Xu, A magnetically recyclable dual Z-scheme GCNQDs-CoTiO3/CoFe2O4 composite photocatalyst for efficient photocatalytic degradation of oxytetracycline, Chemical Engineering Journal 435 (2022) 134833. https://doi.org/10.1016/j.cej.2022.134833.

[58] Y. Matsumoto, Energy Positions of Oxide Semiconductors and Photocatalysis with Iron Complex Oxides, Journal of Solid State Chemistry 126 (1996) 227–234. https://doi.org/10.1006/jssc.1996.0333.

[59] T. Cai, Y. Liu, L. Wang, S. Zhang, Y. Zeng, J. Yuan, J. Ma, W. Dong, C. Liu, S. Luo, Silver phosphate-based Z-Scheme photocatalytic system with superior sunlight photocatalytic activities and anti-photocorrosion performance, Applied Catalysis B: Environmental 208 (2017) 1–13. https://doi.org/10.1016/j.apcatb.2017.02.065.

[60] D. Yadav, R. Gahlawat, R. Shukla, A comprehensive analysis of the impact of annealing temperature variation on the structural, optical, morphological, magnetic, and photocatalytic properties of CoFe2O4 nanoparticles, Ionics 30 (2024) 6559–6574. https://doi.org/10.1007/s11581-024-05713-z.

[61] K.L. Routray, S. Saha, D. Behera, N. Tripathy, S.P. Ghosh, High dielectric constant, low loss and efficient visible photoluminescence properties of porous rose- flower shaped CoFe2O4 for photovoltaic application, Materials Letters 242 (2019) 62–65. https://doi.org/10.1016/j.matlet.2019.01.114.

[62] Y. Jia, Z. Zhou, Y. Wei, Z. Wu, H. Wang, J. Chen, Y. Zhang, Y. Liu, Enhanced photoluminescence of core–shell CoFe2O4/SiO2/Y2O3:Eu3+ composite by remanent magnetization, Smart Mater. Struct. 22 (2013) 125014. https://doi.org/10.1088/0964-1726/22/12/125014.

[63] M. Akhtar, I. Bibi, F. Majid, A. Ghafoor, S. Kamal, G. Fatima, Q. Raza, N. Alwadai, A. Nazir, M. Iqbal, Photoluminescence, structural, optical, ferroelectric and photo-catalytic properties of magnetically separable CdO/CoFe2O4 hetero-junction, Ceramics International (2024) S0272884224002888. https://doi.org/10.1016/j.ceramint.2024.01.272.

[64] M. Goswami, Enhancement of photocatalytic activity of synthesized Cobalt doped Zinc Oxide nanoparticles under visible light irradiation, Optical Materials 109 (2020) 110400. https://doi.org/10.1016/j.optmat.2020.110400.

[65] A. Hassani, A. Khataee, S. Karaca, M. Karaca, M. Kıranşan, Adsorption of two cationic textile dyes from water with modified nanoclay: A comparative study by using central composite design, Journal of Environmental Chemical Engineering 3 (2015) 2738–2749. https://doi.org/10.1016/j.jece.2015.09.014.

[66] A comprehensive review of thermoelectric generation optimization by statistical approach: Taguchi method, analysis of variance (ANOVA), and response surface methodology (RSM), Renewable and Sustainable Energy Reviews 169 (2022) 112917. https://doi.org/10.1016/j.rser.2022.112917.

[67] B.-E. Channab, M. El Ouardi, S.E. Marrane, O.A. Layachi, A. El Idrissi, S. Farsad, D. Mazkad, A. BaQais, M. Lasri, H. Ait Ahsaine, Alginate@ZnCO $_2$ O $_4$ for efficient peroxymonosulfate activation towards effective rhodamine B degradation: optimization using response surface methodology, RSC Adv. 13 (2023) 20150–20163. https://doi.org/10.1039/D3RA02865H.

[68] H. Liang, X. Tai, Z. Du, Photocatalytic degradation of nonylphenol ethoxylate and its degradation mechanism, Journal of Molecular Liquids 302 (2020) 112567. https://doi.org/10.1016/j.molliq.2020.112567.

[69] T.D. Munusamy, C.S. Yee, Md.M.R. Khan, Construction of hybrid g-C3N4/CdO nanocomposite with improved photodegradation activity of RhB dye under visible light irradiation, Advanced Powder Technology 31 (2020) 2921–2931. https://doi.org/10.1016/j.apt.2020.05.017.

[70] A. El Aouni, M. El Ouardi, M. Arab, M. Saadi, H. Haspel, Z. Kónya, A. Ben Ali, A. Jada, A. BaQais, H. Ait Ahsaine, Design of Bismuth Tungstate Bi2WO6 Photocatalyst for Enhanced and Environmentally Friendly Organic Pollutant Degradation, Materials 17 (2024) 1029. https://doi.org/10.3390/ma17051029.

[71] L. Sun, Y. Wang, L. He, J. Guo, Q. Deng, X. Zhao, Y. Yan, K. Qi, Effect of cobalt doping on the photocatalytic performance of AgInS2 for organic pollutant degradation and hydrogen production, Journal of Alloys and Compounds 926 (2022) 166859. https://doi.org/10.1016/j.jallcom.2022.166859.

[72] Z.-Q. Lin, Y. Lai, R.-G. Hu, J. li, R.-G. Du, C. Lin, A highly efficient ZnS/CdS@TiO2 photoelectrode for photogenerated cathodic protection of metals, Electrochimica Acta 55 (2010) 8717-8723. https://doi.org/10.1016/j.electacta.2010.08.017.

[73] Synergistic Effect of CdSe Quantum Dot Sensitization and Nitrogen Doping of TiO2 Nanostructures for Photoelectrochemical Solar Hydrogen Generation | Nano Letters, (n.d.). https://pubs-acs-org.ezproxy.univ-tln.fr/doi/10.1021/nl903217w (accessed November 27, 2024).

[74] S.P. Berglund, F.F. Abdi, P. Bogdanoff, A. Chemseddine, D. Friedrich, R. van de Krol, Comprehensive Evaluation of CuBi2O4 as a Photocathode Material for Photoelectrochemical Water Splitting, Chem. Mater. 28 (2016) 4231–4242. https://doi.org/10.1021/acs.chemmater.6b00830.

View Article Online
DOI: 10.1039/D5CY00951K

[75] L. Jia, N. Ma, P. Shao, Y. Ge, J. Liu, W. Dong, H. Song, C. Lu, Y. Zhou, X. Xu, Incorporating ReS2 Nanosheet into ZnIn2S4 Nanoflower as Synergistic Z-Scheme Photocatalyst for Highly Effective and Stable Visible-Light-Driven Photocatalytic Hydrogen Evolution and Degradation, Small 20 (2024) 2404622. https://doi.org/10.1002/smll.202404622.

[76] B.K. Jha, S. Chaule, J.-H. Jang, Enhancing photocatalytic efficiency with hematite photoanodes: principles, properties, and strategies for surface, bulk, and interface charge transfer improvement, Mater. Chem. Front. 8 (2024) 2197–2226. https://doi.org/10.1039/D3QM01100C.

[77] M.A. Rahman, S. Bazargan, S. Srivastava, X. Wang, M. Abd-Ellah, J.P. Thomas, N.F. Heinig, D. Pradhan, K.T. Leung, Defect-rich decorated TiO_2 nanowires for super-efficient photoelectrochemical water splitting driven by visible light, Energy Environ. Sci. 8 (2015) 3363–3373. https://doi.org/10.1039/C5EE01615K.

[78] H. Feng, S. Feng, N. Tang, S. Zhang, X. Zhang, B. Liu, Fabrication of $TiO_2/Fe_2O_3/CdS$ systems: effects of Fe_2O_3 and CdS content on superior photocatalytic activity, RSC Adv. 11 (2021) 10300–10308. https://doi.org/10.1039/D1RA00195G.

[79] H. Fu, C. Pan, W. Yao, Y. Zhu, Visible-Light-Induced Degradation of Rhodamine B by Nanosized Bi2WO6, J. Phys. Chem. B 109 (2005) 22432–22439. https://doi.org/10.1021/jp052995j.

[80] C. Man, C. Xu, J. Wang, X. Li, T. Li, Y. Ma, S. Zhang, Y. Qiao, Q. Wu, Mechanistic study on the photocatalytic degradation of rhodamine B via Mn–Schiff-base-modified Keggin-type polyoxometalate composite materials, RSC Advances 15 (2025) 12364–12371. https://doi.org/10.1039/D4RA08382B.

[81] H. Zhang, M. Li, W. Wang, G. Zhang, Q. Tang, J. Cao, Designing 3D porous BiOI/Ti3C2 nanocomposite as a superior coating photocatalyst for photodegradation RhB and photoreduction Cr (VI), Separation and Purification Technology 272 (2021) 118911. https://doi.org/10.1016/j.seppur.2021.118911.

View Article Online
DOI: 10.1039/D5CY00951K

Data availability statements

All results are obtained under laboratory research conditions, using equipment equipped with software supplied by the manufacturers (details quoted in the article). Some of the results are summarized in tables, while others are represented in curves.

I hereby inform you that all data are at your disposal and will be provided on request when necessary.

Dr. Madjid Arab (On behalf of all authors)
Université de Toulon, Aix Marseille Univ, CNRS, IM2NP

Dr. Madjid ARAB

M. ARAB